AD-E300 216

DNA 4455F

(12)

ION CLOUD MODELING

Science Applications, Inc.
P.O. Box 2351
La Jolla, California 92038

11 November 1977

Final Report for Period 19 April 1976 — 15 February 1977

CONTRACT No. DNA 001-76-C-0274

APPROVED FOR PUBLIC RELEASE;
DISTRIBUTION UNLIMITED.

THIS WORK SPONSORED BY THE DEFENSE NUCLEAR AGENCY
UNDER RDT&E RMSS CODE B322076464 S99QAXHC04108 H2590D.

Prepared for
Director
DEFENSE NUCLEAR AGENCY
Washington, D. C. 20305

DNA PRINTING PLANT

UNCLASSIFIED

SECURITY CLASSIFICATION OF THIS PAGE (*When Data Entered*)

REPORT DOCUMENTATION PAGE	READ INSTRUCTIONS BEFORE COMPLETING FORM
1. REPORT NUMBER DNA 4455F ✓	2. GOVT ACCESSION NO.
	3. RECIPIENT'S CATALOG NUMBER ⑨
⑥ 4. TITLE (*and Subtitle*) ION CLOUD MODELING.	5. TYPE OF REPORT & PERIOD COVERED Final ~~Report~~ [redacted] 19 Apr 76—15 Feb 77,
	⑭ 6. PERFORMING ORG. REPORT NUMBER SAI-77-918-LJ
⑪ 7. AUTHOR(s) Lewis M./Linson David C./Baxter	⑮ 8. CONTRACT OR GRANT NUMBER(s) DNA 001-76-C-0274
9. PERFORMING ORGANIZATION NAME AND ADDRESS Science Applications, Inc. ✓ P. O. Box 2351 La Jolla, California 92038	⑯ 10. PROGRAM ELEMENT, PROJECT, TASK AREA & WORK UNIT NUMBERS NWED Subtask S99QAXHC041-08
11. CONTROLLING OFFICE NAME AND ADDRESS Director Defense Nuclear Agency Washington, D. C. 20305	⑪ 12. REPORT DATE 11 November 1977
	13. NUMBER OF PAGES 96 ⑫ 92p.
14. MONITORING AGENCY NAME & ADDRESS(*if different from Controlling Office*) ⑰ C041	15. SECURITY CLASS (*of this report*) UNCLASSIFIED
	15a. DECLASSIFICATION/DOWNGRADING SCHEDULE

16. DISTRIBUTION STATEMENT (*of this Report*)

Approved for public release; distribution unlimited.

17. DISTRIBUTION STATEMENT (*of the abstract entered in Block 20, if different from Report*)

⑱ DNA, SBIE ⑲ 4455F, AD E300 1DNA

18. SUPPLEMENTARY NOTES

This work sponsored by the Defense Nuclear Agency under RDT&E RMSS Code B322076464 S99QAXHC04108 H2590D.

19. KEY WORDS (*Continue on reverse side if necessary and identify by block number*)

Barium Release
Ion Cloud
Cloud Density

20. ABSTRACT (*Continue on reverse side if necessary and identify by block number*)

New quantitative procedures are developed for describing the deposition of ion clouds from high-altitude barium releases. The early-time expansion of the neutral vapor cloud via a snowplow model with diffusion added is developed. The inclusion of diffusion provides a description of the evolution of the neutral cloud into a Gaussian shape and provides the basis for a plausible explanation of why the apparent large size of photographic images of early-time expanding neutral clouds are larger than can be → next page

DD FORM 1 JAN 73 1473 EDITION OF 1 NOV 65 IS OBSOLETE

UNCLASSIFIED

SECURITY CLASSIFICATION OF THIS PAGE (*When Data Entered*)

361 6[illegible]2

20. ABSTRACT (Continued)

explained by the release of reasonable amounts of neutral vapor. The subsequent deposition of ionization in the expanding neutral cloud results in an ion cloud that is substantially narrower than the neutral cloud consistent with a number of radar measurements. The influence of neutral winds and settling under gravity on the distribution of ionization along magnetic field lines and the descent through the atmosphere is treated analytically. It is shown that downward winds can delay the decrease in the peak ion concentration and that altitude-dependent winds are more effective in limiting the increase in length of the ion cloud. A quantitative model of the Spruce ion cloud based on these new modeling procedures is developed. The best estimate of the total ion inventory is 6 ± 1 x 10^{24}. The transverse scale of the ion cloud is 2.66 km and the total ion content on the field line passing through the center of the ion cloud is 2.4 x 10^{17} m^{-2}. The peak electron density of 2.45 x 10^{13} m^{-3} is reached at approximately 30 seconds after release and downward neutral winds and/or decreasing atmospheric density scale heights serve to keep the peak ion concentration of the ion cloud above 7 x 10^{12} m^{-3} for more than 30 minutes.

SUMMARY

We have developed a model that quantitatively describes properties of ion clouds produced from barium releases in the lower ionosphere. First, a quantitative procedure is described for the formation of the ion cloud from the expanding cloud of neutral barium vapor. Second, the subsequent expansion of the ion cloud along magnetic field lines and its descent through the atmosphere under the influence of gravity and neutral winds is treated analytically. Third, the results of these procedures are applied towards determining quantitative characteristics of the Spruce ion cloud.

A description of the early-time expansion of the neutral barium-atom vapor cloud is described by a snowplow model with diffusion added. The addition of diffusion aids in making the transition from an early rapidly-expanding dense cloud to a late-time cloud that is expanding solely by diffusing through the ambient atmosphere. It is shown that the effect of diffusion is to rapidly change an arbitrary initial density distribution into a Gaussian distribution which then begins to increase the radius of the neutral cloud.

A detailed examination of the results of the theoretical model in comparison with a film record of the Spruce neutral cloud at 20 seconds after release is made. This comparison provides a plausible explanation for the observed fact that photographic images of early-time neutral clouds appear to be far larger than could readily be explained by the release of reasonable amounts of barium vapor. Previous modeling attempts have required the assumption that more than twice the amount of vapor was released than is assumed in this report.

The subsequent deposition of the ion cloud from the expanding neutral vapor cloud is treated quantitatively. The results show the ion cloud is substantially narrower than the neutral cloud. The result of this model deposition is to produce an ion cloud with transverse widths which are in substantial agreement with radar measurements of the transverse scale size of the early-time ion cloud. We find that the high-density central portion of the ion cloud is more peaked than a Gaussian distribution, but that the outer regions contain far more ionization than a Gaussian contains.

The subsequent development of the ion cloud along magnetic field lines and its descent through the ambient atmosphere is treated analytically. The treatment includes a magnetic field of arbitrary dip angle, the presence of neutral winds, and examines the responses of both low- and high-conductivity ion clouds. It is found that the time to assume an asymptotic shape is substantially longer than had been estimated previously. Downward neutral winds can substantially delay the decrease in the peak ion density and the spread of the ion cloud. Altitude-dependent neutral winds appear to have a greater effect in limiting the increase in length of the ion cloud. Moderate upward winds do not increase the altitude of the peak electron concentration, but are effective in bringing substantial amounts of ionization to higher altitudes.

A quantitative model of the Spruce ion cloud is developed that is in substantial agreement with most of the reliable measurements of barium ion clouds produced from 48 kg chemical payload releases at around 190 kilometers altitude. The best estimate of the total ion inventory developed here for the Spruce ion cloud is $6 \pm 1 \times 10^{24}$. Detailed models A, B and C are developed in order to illustrate the variations produced by different assumptions. The basic model A has a scale size transverse to the magnetic field of 2.66 km and a total field-line content through the center of the cloud of 2.4×10^{17} m^{-2}. It reaches its maximum electron concentration of 2.45×10^{13} m^{-3} at approximately 30 seconds after release. The subsequent expansion and descent of the ion cloud is shown graphically. Model B has the same initial conditions as model A but shows that downward neutral winds and/or a decreasing neutral-density scale-height can maintain the peak electron concentration above 7×10^{12} m^{-3} for longer than 30 minutes after release. Model C presents an underestimate of the total ion inventory that is forced to agree precisely with two early-time radar measurements of the peak electron densities which in model A are treated as lower bounds.

TABLE OF CONTENTS

LIST OF ILLUSTRATIONS

LIST OF TABLES

1. INTRODUCTION AND SUMMARY

In order to model the characteristics of striations that have developed from barium releases, it is important to know the original configuration of ionization in the ion cloud out of which the striations are formed. The electron densities and distribution of scale sizes that exist in the striations at late time when they are well-developed depend on these initial conditions. It is the purpose of this report to describe a procedure for developing a model of the initial ion cloud and to apply that procedure to the Spruce ion cloud that was released February 1, 1971 as part of the Secede II Test Series.

As described in more detail below, three aspects of developing a description of the ionization in the ion cloud are treated in the next three sections of this report. First, the expansion of the barium neutral cloud which consists almost entirely of vaporized barium atoms is treated. Second, the deposition of ionization resulting from photoionization of the barium atoms in the expanding neutral cloud is calculated. These two topics are treated in Sections 2 and 3 and result in a description of the characteristics of the ion cloud at early time. The behavior of the cloud at late time, that is, its transport due to neutral winds and electric fields and its change in shape along magnetic field lines and descent into the neutral atmosphere, is treated in Section 4. In the last section of the report the results of these modeling procedures are applied to develop quantitative models of the Spruce ion cloud.

We will be treating several aspects of the continuity equation for ions written in the form

$$\frac{\partial n}{\partial t} + \nabla_{\perp} \cdot n\vec{v}_{i\perp} + \frac{\partial}{\partial z} n v_{iz} = S(\vec{r}, t) \qquad (1.1)$$

where n is the ion concentration, $\vec{v}_{i_\perp}$ and v_z are components of velocity transverse and parallel to the magnetic field and $S(\vec{r}, t)$ is the source function describing the creation of ionization. In Section 2 we describe a procedure for calculating the source function $S(\vec{r}, t)$. In Section 3 we neglect the second term on the left-hand side, that is, the transverse transport of ionization across magnetic field lines, and solve the remaining parts of the continuity equation at early time during the first minute following release when $S(\vec{r}, t)$ is nonzero. In Section 4 we describe the behavior of the ion cloud beyond one minute after release when the right-hand side of Eq. (1.1) is equal to zero under the assumption that the ion cloud moves as a whole across magnetic field lines.

There are several motivations for carrying out the investigation described in this report. These motivations can be best expressed by asking several questions. How can the apparent large size of the photographic image of neutral clouds be reconciled with the release of only reasonable amounts of barium vapor? How can radar measurements of the transverse dimension of the early-time ion cloud be consistent with the larger size of the expanding neutral cloud? How quickly can ion clouds descend to low altitudes and can the peak ion concentration* increase at late time? The analyses carried out in Sections 2, 3 and 4 provide satisfactory answers to these questions.

In Section 2 a description of the expanding neutral barium atom vapor cloud is provided. The expansion proceeds via a snowplow model with diffusion added. The inclusion of diffusion is a new feature and provides a description of the transition of the initial rapid expansion of an arbitrary initial density configuration into a Gaussian profile that is expanding by diffusing through the ambient atmosphere at late time. The effect of diffusion is to change an arbitrary initial density profile into a Gaussian profile.

We have carried out a detailed analysis of the intensity profile recorded on a photographic film of the Spruce neutral cloud at 20 seconds after release.

---

*Electron concentration and ion concentration are equal to each other and will be used interchangeably throughout this report. Electron density or ion density is sometimes used to mean the same quantity.

This profile is compared with the shapes that are predicted from our theoretical treatment of snowplow plus diffusion. We find that both the scale size and the shape predicted by the theoretical model are in reasonable agreement with the photographic record when interpreted properly. Hence, we believe that we have provided a plausible explanation for the apparent large photographic image of neutral clouds during the first tens of seconds after release. Previous theoretical treatments of this problem[1, 2] have assumed that unreasonably large amounts of neutral barium atom vapor were produced in order to match the size of the early-time images of neutral clouds.

Section 3 provides a description of the deposition of ionization by the photoionization of the neutral barium atoms in the expanding neutral cloud. As a result of this procedure it is found that the scale size of the ion cloud transverse to the magnetic field is considerably smaller than the neutral cloud radius. The central high-density portion of the ion cloud is more peaked than a Gaussian distribution but the outer edges fall off less rapidly than do a Gaussian and contain a far greater inventory of ions.

In Section 4 several aspects of the motion of barium ion clouds are treated. General equations are derived for the motion of both low- and high-conductivity ion clouds. These equations incorporate several features not ordinarily included that have a bearing on the subject of the behavior and motion of the ion cloud. They include a neutral atmosphere whose density is a function of altitude, and the presence of a neutral wind that is not necessarily spatially uniform. The effect of gravity and a magnetic field with an arbitrary dip angle is also included.

Low-conductivity ion clouds are transported across magnetic field lines solely by ambient electric fields which produce $\vec{E} \times \vec{B}$ motion. The presence of a neutral wind tends to slide the ion cloud along the magnetic field lines. Neutral winds have a greater effect on the transport of higher conductivity ion clouds across magnetic fields. Indeed, in the limit of very high conductivity, the ion cloud moves as though the magnetic and electric fields were not present. The magnetic field serves solely to align the ion cloud.

Both gravity and the component of the neutral wind parallel to the magnetic field have a large effect on the distribution of ionization parallel to the magnetic field. The changes in the distribution of ionization and descent of the ion cloud are computed explicitly for various examples of vertical neutral winds. It is found that downward winds decrease the rate at which the ion cloud spreads parallel to the magnetic field and thereby lessens the decrease in the peak ion content.

In Section 5 we apply these modeling procedures to the Spruce ion cloud. A quantitative model is developed that is in substantial agreement with most of the reliable measurements of barium ion clouds produced from 48 kg chemical payload weight releases at around 190 km altitude. The best estimate of the total ion inventory developed here for the Spruce ion cloud is $6 \pm 1 \times 10^{24}$. Detailed models A, B and C are developed in order to illustrate the variations produced by different assumptions. The basic model A has a scale size transverse to the magnetic field of 2.66 km and a total field-line content through the center of the cloud of 2.4×10^{17} m^{-2}. It reaches its maximum electron concentration of 2.45×10^{13} m^{-3} at approximately 30 seconds after release. The subsequent expansion and descent of the ion cloud is shown graphically. Model B has the same initial conditions as model A but shows that downward neutral winds and/or a decreasing neutral-density scale-height can maintain the peak electron concentration above 7×10^{12} m^{-3} for longer than 30 minutes after release. Model C presents an underestimate of the total ion inventory that is forced to agree precisely with two early-time radar measurements of the peak electron concentration which in model A are treated as lower bounds.

2. NEUTRAL CLOUD EXPANSION

2.1 INTRODUCTION

In order to properly model the characteristics of the ion cloud (size, electron concentration,* etc) produced from barium releases, it is necessary first to model the behavior of the expanding neutral cloud. The distribution of ionization in the ion cloud can then be calculated by using the neutral cloud distribution as a source for the production of barium ions.

In an earlier work[1] the expansion of the neutral cloud was modeled in three separate stages. In the first stage, the gas release is slowed down solely by losing momentum to the surrounding air via a snowplow model. In the second stage the neutral cloud continues to expand depending on the range or mean free path of the barium atoms in the ambient air. After a few seconds during which the initial kinetic energy of expansion has been dissipated, the neutral atoms continue to spread by diffusing through the ambient air.

There are a number of fundamental problems associated with some of the assumptions that were made in developing that model. First, it was assumed that the vaporization efficiency of barium atoms was 30% of the available excess barium contained in the chemical payload. This efficiency is greater than has ever been reliably measured. Furthermore, it was assumed that the mass of the expanding neutral cloud was 20% of the total chemical payload weight amounting to a mass approximately 40% more than the mass of the barium vapor. There is no other species in significant amounts other than small amounts of the impurity strontium to account for this extra mass. These unjustified assumptions were motivated by the apparent large optical size of the neutral cloud at early time. We will discuss in detail how more reasonable assumptions regarding the mass of vapor produced can be consistent with optical data.

---

*See footnote on page 8.

The simplified snowplow model adopted earlier did not properly conserve momentum and energy. We will use a more appropriate snowplow model here. The earlier description of the transition from the initial snowplow regime to the later diffusion regime was at best heuristic. We will formally introduce diffusion into the snowplow model which allows assumed initial density distributions to evolve into a Gaussian shape.

The results of the former modeling were to produce ion clouds that contained a larger ion inventory and had characteristic transverse dimensions larger than now believed to be reasonable. The principal success of the former modeling effort which speaks in its favor was that it did predict the correct change in size of the ion cloud and the peak electron densities achieved by a series of different size releases conducted at different altitudes. The variation in chemical payloads ranged over two and one-half orders of magnitude and the background atmospheric density varied by a factor of twenty. We shall show how the modifications in the description of the expansion of the neutral cloud mentioned above lead to neutral and ion clouds whose physical properties are consistent with available data.

2.2 SNOWPLOW MODEL WITH DIFFUSION

We have investigated the early-time behavior of the expanding neutral gas cloud by using an extension of a snowplow model introduced by Stuart[3] in 1965. Much of our development of this model was done in connection with other work relating to the release of gas clouds at satellite orbital velocities,[4] but the specific modification of considering the effect of high release velocity is not relevant to this problem.

In this model all lengths scale with a characteristic length called the equal-mass-radius, a_0. This length is the radius of a spherical volume of ambient atmosphere with mass equal to the mass of the released gas, M_0. In terms of the ambient atmospheric density, ρ_a, the equal-mass-radius is defined by $a_0 = (3M_0/4\pi\rho_a)^{1/3}$. The central assumptions of Stuart's model are that a spherical cloud of gas, consisting of released gas plus swept up ambient atmosphere, retains a self-similar or shape-preserving density profile, that the velocity of the gas is radial, and that the velocity increases linearly with radius from the center of the cloud.

This model appears to be appropriate when $3 < a_o/\lambda < 30$ where λ is the ambient mean-free-path between collisions. Since $a_o \sim$ 1-2 km for 48 kg barium releases at around 190 km altitude and $\lambda \sim$ 100-200 m, this model which treats the released vapor and ambient atmosphere as being well-mixed but still subject to a fluid treatment is appropriate. At higher altitudes where $a_o < 3\lambda$ a kinetic treatment would be necessary. At lower altitudes where $a_o > 30\lambda$, it is difficult to consider the released and ambient species as being well-mixed and other gasdynamic phenomena neglected in the snowplow treatment, such as shock formation and wave generation, would be dominant.

In this work we modify the Stuart model to include the fact that at late time the gas cloud can be modeled by a Gaussian density profile diffusing into the ambient atmosphere. The result is a model which initially follows a Stuart snowplow expansion and evolves into a Gaussian diffusing cloud. Obviously, we must relax one of the central assumptions of the Stuart model, specifically that the cloud retains a shape-preserving density profile. We will treat the effect of diffusion as if it were superimposed on the expansion process modeled by the self-similar snowplow expansion. In a self-similar expansion the size of the cloud is given by R(t), a time-dependent scale length of the cloud. If the self-similar shape were a spherical constant-density profile, for example, we would take R(t) to be equal to the radius of the sphere.

We use this same R(t) to scale the continuity equation for mass, as was used in the development of Stuart's model, with the addition of a term due to diffusion;

$$\frac{D\rho}{Dt} + \rho \nabla \cdot \vec{v} = D_n \nabla^2 \rho + \frac{\dot{M}}{M} \rho \qquad (2.1)$$

where the hydrodynamic derivative is given by

$$\frac{D}{Dt} = \left(\frac{\partial}{\partial t}\right)_r + \vec{v} \cdot \nabla \ , \tag{2.2}$$

$\vec{v}$ is the fluid velocity of the gas given by $\vec{v} = \vec{r}\dot{R}/R$, where $R(t)$ is the characteristic scale length of the expanding cloud if there were no diffusion, ρ is the mass density and $M(t)$ is the total mass of the gas cloud including the swept-up ambient mass. The dot indicates differentiation with respect to time. D_n is the diffusion coefficient which was not included in earlier treatments of the Stuart model. The last term on the right-hand-side of Eq. (2.1) includes the effect of sweeping up ambient mass according to Stuart's original model.

By making a suitable change of space and time variables we can define a function $f(\vec{\xi}(r,t), \tau_D(t))$ which is analogous to the shape function of the self-similar model. If we define $\vec{\xi}$ and τ_D by

$$\vec{\xi} = \vec{r}/R(t) \quad ;$$

$$\tau_D = \int_{t_D}^{t} \frac{4D_n\, dt}{R^2(t)} \quad ; \tag{2.3}$$

implying that diffusion begins at $t = t_D$, then the density can be written

$$\rho(\vec{r},t) = \left[M(t)/R^3(t)\right] f\left[\vec{\xi}\,(\vec{r},t),\ \tau_D(t)\right] \ .$$

With these substitutions Eq. (2.1) can be simply written

$$\frac{\partial f}{\partial \tau_D} = \frac{1}{4} \nabla_\xi^2 f \tag{2.4}$$

where we have used the following:

$$\vec{v} = \frac{\dot{R}}{R} \vec{r} \ ;$$

$$\vec{\nabla} \cdot \vec{v} = 3\,\dot{R}/R \ ;$$

$$\frac{\partial\rho}{\partial t} = \frac{\dot{M}}{R^3} f - 3\frac{M\dot{R}}{R^4} f + \frac{M}{R^3}\frac{\partial\vec{\xi}}{\partial t}\cdot\nabla_\xi f + \frac{M}{R^3}\frac{\partial\tau_D}{\partial t}\frac{\partial f}{\partial\tau_D} \quad ;$$

$$\nabla\rho = \frac{M}{R^4}\nabla_\xi f \quad ;$$

$$\nabla^2\rho = \frac{M}{R^5}\nabla_\xi^2 f \quad ;$$

$$\frac{\partial\vec{\xi}}{\partial t} = -\dot{R}\,\vec{r}/R^2 \quad ;$$

$$\frac{\partial\tau_D}{\partial t} = \frac{4D_n}{R^2(t)} \quad .$$

Equation (2.4) is the diffusion equation for $f(\vec{\xi},\tau)$, which has the solution

$$f\left(\vec{\xi},\tau_D\right) = \int d^3\vec{\xi}\,'\, f(\vec{\xi}\,',0)\,\frac{\exp\left(-(\vec{\xi}-\vec{\xi}\,')^2/\tau_D\right)}{\left(\pi\,\tau_D\right)^{\frac{3}{2}}} \quad . \tag{2.5}$$

In terms of this function we may write the density at any time $t > t_D$ as

$$\rho(\vec{r},t) = \frac{M(t)}{R^3(t)}\frac{1}{M_D}\int d^3r'\,\rho\left(r',t_D\right)\frac{\exp\left(-\left(\frac{\vec{r}}{R}-\frac{r'}{R_D}\right)^2/\tau_D(t)\right)}{\left(\pi\,\tau_D(t)\right)^{\frac{3}{2}}}$$

where $R_D = R(t_D)$ and $M_D = M(t_D)$. For $\tau_D << 1$ we have the limit of little diffusion and the density reduces to that given by the self-similar model,

$$\rho(r,t) = \frac{M}{M_D}\frac{{R_D}^3}{R^3}\,\rho\left(r\frac{R_D}{R},\, t_D\right)$$

or

$$\rho(r,t) = \frac{M}{R^3} f(r/R,\ 0) \quad .$$

At long times after diffusion has been turned on the similarity function f approaches a Gaussian distribution with an expanding radius and constant volume:

$$f\left(\xi, \tau_D\right) \rightarrow \left(\pi \tau_D\right)^{-\frac{3}{2}} \exp\left(- \xi^2/\tau_D\right) \tag{2.6}$$

as $\tau_D \rightarrow \infty$.

In order to illustrate the effect that diffusion in ξ has on an assumed density distribution, we have applied Eq. (2.5) to two specific examples. The first is a uniform density out to a finite expanding radius; we refer to this shape as a flat-top distribution. The second is an expanding spherical shell with all the mass concentrated at the surface of the shell. For the flat-top distribution

$$f(\xi, 0) = 3/4\pi \quad ; \quad \xi < 1$$

$$f(\xi, 0) = 0 \quad ; \quad \xi > 1 ,$$

and for the spherical shell

$$f(\xi, 0) = \delta(\xi - 1)/4\pi .$$

The normalization has been chosen so that each contains a unit volume.

We have found that the approach to a Gaussian profile takes place more rapidly if the Gaussian radius has the form $\left(\alpha + \tau_D\right)^{\frac{1}{2}}$ instead of $\tau_D^{\frac{1}{2}}$, i.e.,

$$f\left(\xi, \tau_D\right) \rightarrow \left[\pi\left(\alpha+ \tau_D\right)\right]^{-\frac{3}{2}} \exp\left[-\xi^2/\left(\alpha + \tau_D\right)\right] . \tag{2.7}$$

In order to illustrate the change of the flat-top and spherical-shell distribution toward the Gaussian form given in Eq. (2.7) at various values of τ_D , we have renormalized both the radius and density by defining

$$z = \xi / \left[0.693\left(\alpha + \tau_D\right)\right]^{\frac{1}{2}}$$

$$g\left(z, \tau_D\right) = \left[\pi\left(\alpha + \tau_D\right)\right]^{\frac{3}{2}} f\left(\xi, \tau_D\right) \quad . \qquad (2.8)$$

The limiting value of $g(z, \tau_D)$ for large τ_D is $\exp(-0.693 z^2)$. The scale factor 0.693 is chosen so that $g(1, \infty)$ is 0.5.

Figures 2.1 and 2.2 show $g(z, \tau_D)$ for various values of τ_D for the flat-top and spherical shell initial distributions respectively. The value of α in the scalings given by Eq. (2.8) are different for the two cases. It is appropriate that α be unequal to zero because in both cases the initial shapes have finite spatial extent. We have chosen α so that $g(1, 1)$ is approximately equal to one half; for the flat-top $\alpha = 0.5$ and for the spherical shell $\alpha = 0.75$. The larger value of α for the spherical shell results from the fact that all of the mass is initially at $\xi = 1$ for the shell while the mass is distributed over $\xi \leq 1$ for the flat-top.

The vertical dashed lines in Figures 2.1 and 2.2 indicate the position of the initial radius in the newly-scaled length coordinate z . For τ_D greater than one, the position of the initial radius moves to the left and approaches $z = 1.2\, \tau_D^{-\frac{1}{2}}$ as $\tau_D \rightarrow \infty$ indicating the increase in size of the cloud due to diffusion. For the flat-top in Figure 2.1, the horizontal dashed lines indicate the height of the original flat-top in the newly-scaled density with amplitude $[\pi(\alpha + \tau_D)]^{\frac{3}{2}} f(\xi, 0)$.

Examination of Figures 2.1 and 2.2 indicates that the density distributions are approaching Gaussian-like shapes for $\tau_D > 0.2$ and 0.75 for the two cases, respectively, and have essentially the asymptotic shape given in Eq. (2.7) for $\tau_D > 0.4$ and 1.0 respectively. We will discuss specific evaluations of τ_D in the next subsection.

The approximation of $f(\xi, \tau_D)$ by its limiting form $[\pi(\alpha + \tau_D)]^{-\frac{3}{2}} \times \exp[-\xi^2/(\alpha + \tau_D)]$ is equivalent to approximating the density distribution of the cloud by a Gaussian density profile

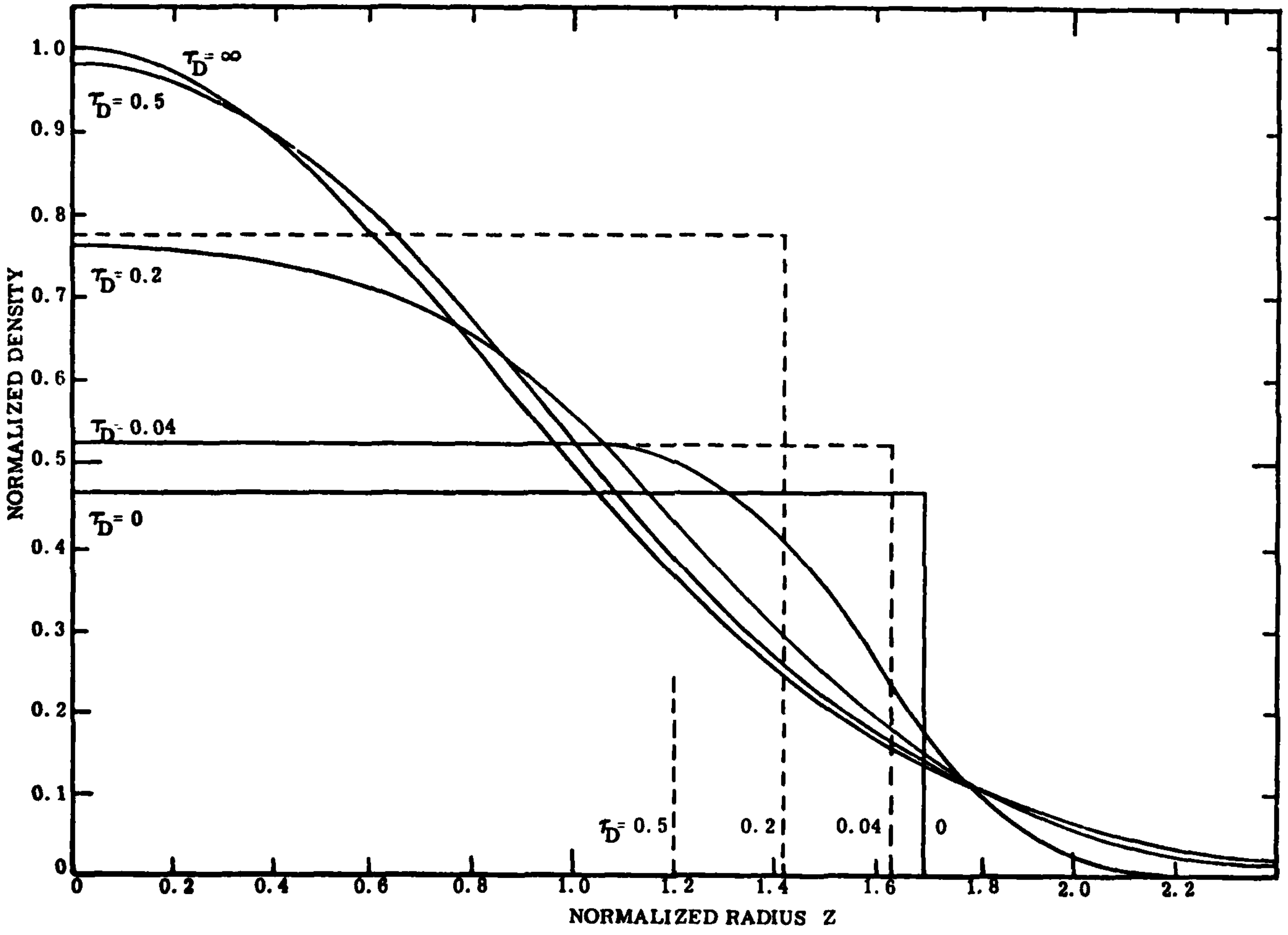

Figure 2.1. The evolution of the normalized density distribution from an initial flat-top to a Gaussian as a result of diffusion for several values of the diffusion parameter τ_D.

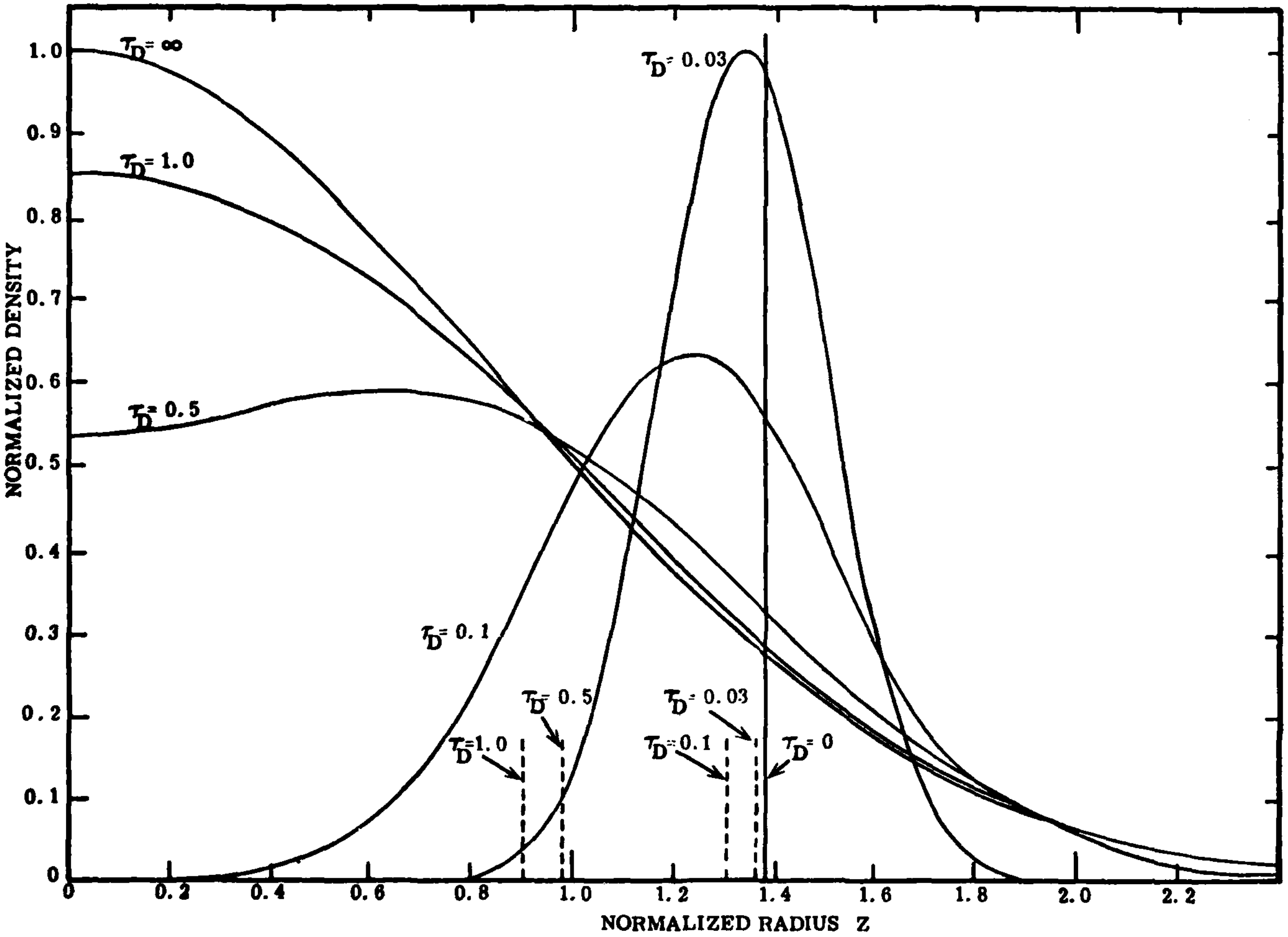

Figure 2.2. The evolution of the normalized density distribution from an initial shell to a Gaussian as a result of diffusion for several values of the diffusion parameter τ_D.

$$\rho(r,t) \sim M(t) \left[\pi a^2(t)\right]^{-\frac{3}{2}} \exp\left[- r^2/a^2(t)\right] \qquad (2.9)$$

with a time-dependent Gaussian radius, $a(t)$, given by

$$a^2(t) = R^2(t) \left[\alpha + \tau_D(t)\right] \qquad (2.10)$$

where τ_D is given by Eq. (2.3). Although the actual shape at early time is not Gaussian, in the case of the flat-top distribution we find that the distance at which the density is 1/e of its value at $r = 0$ is within a few percent of $R(t)$ for $\tau_D(t) < 0.5$ and of course is indistinguishable from $a(t)$ given by Eq. (2.10) for $\tau_D > 0.5$.

In the preceding, we have discussed a procedure for introducing diffusion within the framework of a snowplow model. The effect of diffusion is to transform an initial self-similar profile for the density into a Gaussian profile. The treatment so far does not depend on the time-dependence of $R(t)$ which we take to be determined by the snowplow model without diffusion.

Using local conservation of mass and momentum and global conservation of energy, the Stuart snowplow determines a function $\phi(s)$ such that

$$R(t) = a_0 \phi(s) \qquad (2.11)$$

and

$$s = \dot{R}_0 t/a_0 \qquad (2.12)$$

where $\dot{R}_0$ is the initial expansion velocity of $R(t)$.

Our normalizations for ϕ and s are different from those of Stuart; with our normalizations ϕ satisfies the differential equation:

$$\phi \frac{d}{ds} \left[\left(1 + \phi^3\right) \frac{d\phi}{ds}\right] = \frac{3(\gamma - 1)}{2} \left[1 - \left(1 + \phi^3\right) (d\phi/ds)^2\right]$$

where γ is the ratio of specific heats. The solution of this equation has the following properties for large and small s :

$$\phi(s) \rightarrow s \qquad\qquad \text{for } s << 1$$

$$\phi(s) \rightarrow \left(6.25\,\frac{\gamma - 1}{\gamma}\right)^{0.2} s^{0.4} \qquad \text{for } s >> 1$$

At early time the cloud expands with the initial expansion velocity $\dot{R}_o$ while at later time the cloud radius is predicted to expand as $t^{0.4}$. At very late time when the snowplow description is no longer appropriate, the cloud expands as $t^{0.5}$ due to diffusion. It is apparent that once the appropriate value of γ of the released gas is specified, the snowplow model for the expansion of a gas cloud determines the time-dependence of the radius $R(t)$ of the cloud in terms of the two key parameters a_o and $\dot{R}_o$.

Once the functional dependence of $\phi(s)$ is known, then we may define a normalized diffusion function $\bar{\tau}(s)$ by

$$\bar{\tau}(s) = \int_1^s \frac{ds}{\phi^2(s)} \quad . \tag{2.13}$$

The diffusion parameter τ_D defined in Eq. (2.3) can be expressed in terms of $\bar{\tau}(s)$ as

$$\tau_D(t) = \frac{4D_n}{a_o \dot{R}_o}\left[\bar{\tau}(s) - \bar{\tau}(s_D)\right] \tag{2.14}$$

where $s = \dot{R}_o t/a_o$ and the diffusion is assumed to commence at $t = t_D$. For a gas with $\gamma = 5/3$ which is appropriate for barium atom vapor, we show the resulting normalized diffusion function $\bar{\tau}(s)$ in Figure 2.3. The solid curve is the correct value of $\bar{\tau}(s)$ only as long as $\phi(s)$ is given by the snowplow model. If the snowplow model were to be turned off at a specific value of s, then ϕ^2 in the denominator would be a constant and ϕ would increase linearly with s. Examples are shown by the dashed curves in Figure 2.3 if the snowplow were stopped at $s = 18$ and 46. We will discuss specific

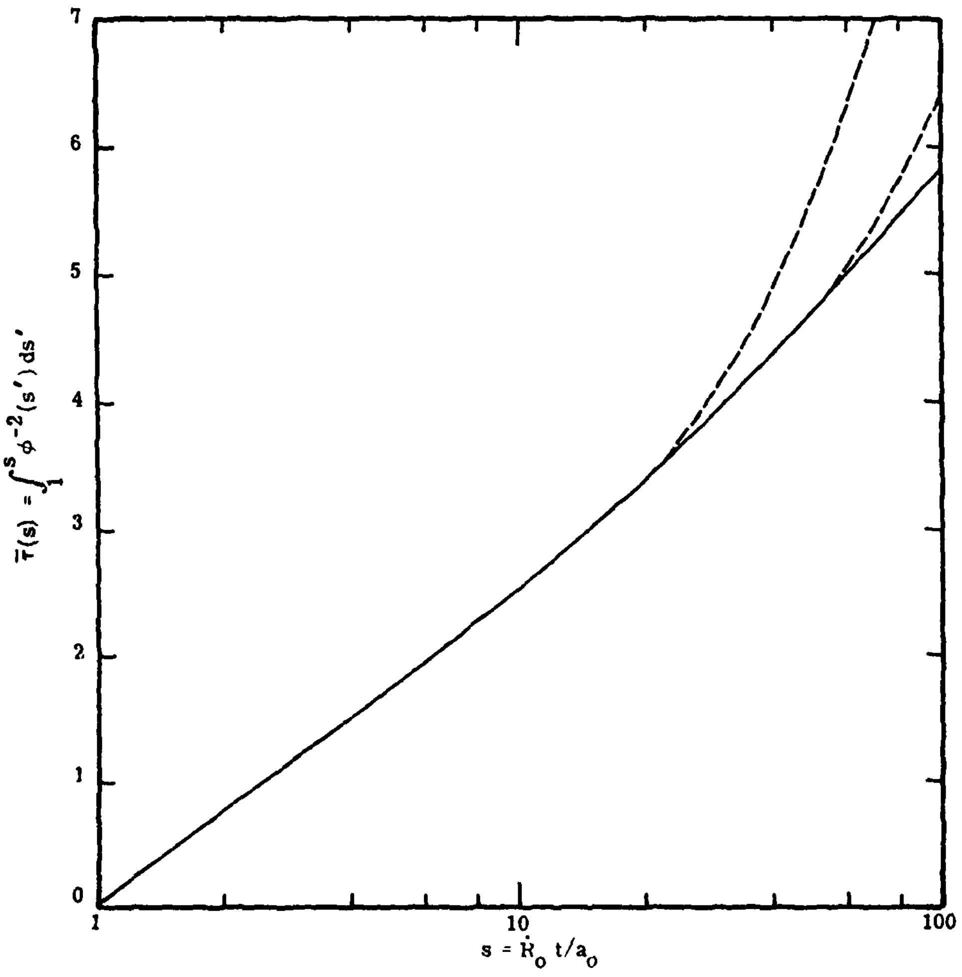

Figure 2.3. Normalized diffusion function $\bar{\tau}(s)$ for a gas with $\gamma = 5/3$ in terms of which the diffusion parameter τ_D is defined according to Eq. (2.14). The dashed curves show the values of $\bar{\tau}(s)$ if the snowplow were stopped at $s = 18$ and 46 respectively.

numerical values for the expansion and diffusion of the Spruce neutral cloud in the following subsection.

2.3 EXPANSION AND SHAPE OF THE NEUTRAL CLOUD

In Section 5 of this report we will present parameters that define two early-time models of the Spruce ion cloud. Model A and model C represent ion clouds whose ion inventories are an upper estimate and an underestimate, respectively. The model parameters listed there are believed to be valid because they are consistent with the model of the neutral gas cloud expansion described in the previous subsection and consistent with a detailed analysis of a film record of the Spruce neutral cloud to be described here.

In order to compare the results of the theoretical description with the observation of the Spruce neutral cloud, we will use the values appropriate for model A. A discussion of the sensitivity of the adopted model values to various assumptions will be deferred to Section 5.

The Spruce cloud was released on 1 February 1971 at 2352 UT at an altitude of about 190 km from Eglin AFB in Florida. The CIRA 1965 atmospheric model 6 at 1800 hours, appropriate for the solar flux conditions that existed during the second half of January 1971, was used to obtain the following parameters at 190 km altitude:

ambient mass density $\rho_a = 0.45 \text{ kg/km}^{-3}$;
neutral air temperature $T_n = 1086° \text{ K}$;
barium ion-neutral collision time $\tau = 0.8 \text{ s}$;
barium-neutral diffusion coefficient $D_n = k\, T_n\, \tau/M = 0.052 \text{ km}^2/\text{s}$;

The barium-neutral collision time is discussed in Section 4.4.

The chemical formulation for the barium thermite is based on the reaction of 2.5 moles of barium per mole of cupric oxide according to the formula

$$2.5\, Ba + CuO \rightarrow BaO + Cu + 1.5\, Ba .$$

In addition, 1.8% of the thermite weight was barium azide.[5] As a result, roughly half (47.8%) of the chemical payload weight was available as excess barium, amounting to 1.01×10^{26} barium atoms per 48-kg barium release. The results of model A for the ion cloud discussed in Section 5 indicate that approximately 15.5% of the available barium, or $M_o = 3.56$ kg, exits the cannister as barium atoms. We note that this corresponds to an efficiency by weight of 7.4% which is right in the middle of the usual estimate of 5 to 10%. Measurements of the initial expansion velocity report typical values between 1.0 and 1.4 km/s. For model A we have adopted the value 1.15 km/s for the initial expansion velocity $\dot{R}_o$.

We have now specified the parameters necessary to apply the theoretical model developed in the previous subsection to observations of the neutral cloud. By using the above mass of released vapor, we determine the equal-mass-radius for model A to have the value $a_o = 1.26$ km. The dimensionless coefficient of the diffusion parameter τ_D in Eq. (2.14) has the numerical value $4\, D_n / a_o \dot{R}_o = 0.144$.

The solid curve in Figure 2.4 shows the radius of the Spruce neutral cloud as a function of time after release according to the snowplow model. Since the radius and time are given on a logarithmic scale, the solid curve also represents the function $\phi(s)$ shifted horizontally by the scale factor $a_o/\dot{R}_o$ and vertically by the factor a_o . We have found that the function

$$\tilde{\phi}(s) = \left(1.44\, s^{0.8} - 0.63\right)^{\frac{1}{2}} \qquad (2.15)$$

is indistinguishable from $\phi(s)$ for $s > 1$ and have used $\tilde{\phi}(s)$ in carrying out calculations involving $\phi(s)$. The radius of the neutral cloud as a function of time is then given by

$$R(t) = a_o \left[1.44 \left(\frac{\dot{R}_o t}{a_o}\right)^{0.8} - 0.63\right]^{\frac{1}{2}} . \qquad (2.16)$$

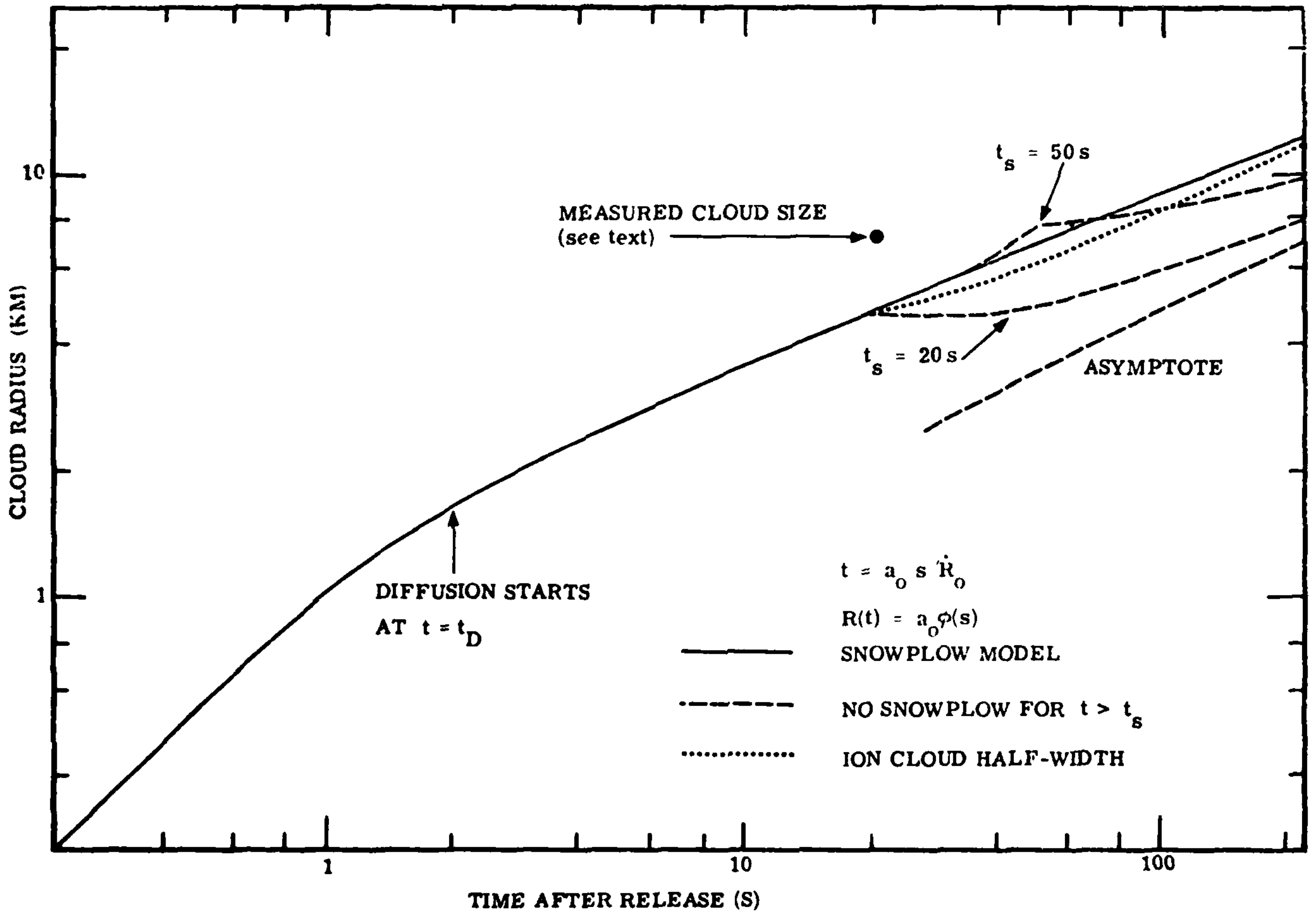

Figure 2.4. Neutral gas cloud radius as a function of time after release according to model A with $a_o = 1.26$ km and $\dot{R}_o = 1.15$ km/s. The dashed curves show the effect of suddenly turning off the snowplow at 20 s and 50 s.

The neutral cloud reaches the equal-mass-radius of 1.26 km at $s = 1.16$ or at around 1.3 seconds after release. At this time the expanding barium-vapor cloud has picked up a mass of ambient air equal to the mass of the expanding vapor. It would seem inappropriate to introduce diffusion as an important mechanism for times earlier than this time. For illustrative purposes we have started diffusion a little later at around 2 seconds after release when s has the value of 1.8.

According to the discussion in the previous subsection, diffusion initially does not increase the size of the neutral cloud. Until $\tau_D = 0.5$, it serves primarily to evolve an initial flat-top distribution into a Gaussian shape. During this time the radius of the cloud given by the solid curve or Eq. (2.16) gives the dimension of the point on the neutral cloud that has a value 1/e of its value at $r = 0$.

The dashed curves in Figure 2.4 show the effect of suddenly turning off the snowplow model at $t = 20$ s and $t = 50$ s after release. According to the snowplow model the neutral cloud 1/e radius has a value of 4.72 km at 20 s and the dimensionless time parameter s has the value 18 . The diffusion parameter τ_D can be evaluated by using its definition in Eq. (2.14), the numerical value 0.144 for the coefficient $4\, D_n/a_o \dot{R}_o$, and Figure 2.3 for $\bar{\tau}(s)$. We find that τ_D is approximately 0.4 at 20 s after release and reaches the value of 0.5 at around 35 s after release. We should remark that the solid curve in Figure 2.3 is valid only during the time that the snowplow is describing the time dependence of $R(t)$.

If the snowplow were turned off at 20 s after release, diffusion would cause the neutral cloud to continue to evolve toward a Gaussian but would not increase its size for the next 10 to 15 seconds. At this time when τ_D reached the value 0.5, the neutral cloud would begin to increase in size. On the other hand, if we delayed the turnoff of the snowplow until 50 s after release, diffusion would increase the size of the neutral cloud between 35 and 50 s as shown. After the sudden turnoff at 50 s , the neutral cloud would continue to expand by diffusion. We note that both dashed curves are approaching the dashed curve labeled asymptote which at late time gives the Gaussian radius of the neutral cloud as $4D_n t$. Of course, the sudden turnoff of the snowplow is unphysical; in actuality it gradually ceases to contribute to the increase in size of the neutral cloud. Measurements of the images of neutral clouds on photographic plates tend to show that during the time period from 20 to 100 seconds after release they do not increase in size very rapidly. We believe that this is a reflection of the fact that the snowplow model is no longer an appropriate description for the increase in size of the neutral cloud at this late time.

In Section 5, we will discuss the increase in size of the ion cloud. For reference purposes the dotted line in Figure 2.4 shows the Gaussian half-length of the ion cloud parallel to the magnetic field. This curve is derived by assuming that the ion cloud increases in length according to the formula

$$\ell^2(t) = (4.72)^2 + 4D_o(t - 20) \quad \text{km}^2 \tag{2.17}$$

where D_o is the parallel diffusion coefficient,

$$D_o = k\left(T_e + T_i\right)\tau/M = \left(\left(T_e + T_i\right)/T_n\right)D_n \quad .$$

For ion temperatures equal to the neutral temperature and electron temperatures 30% hotter, D_o has the value 0.12 km^2/s .

2.4 COMPARISON WITH OBSERVATION OF THE SPRUCE NEUTRAL CLOUD

Boquist et al.[6] have reported a measurement of the radius of the Spruce neutral cloud at 20 seconds after release of 7.2 km. This measured size is shown as a dot in Figure 2.4. This measurement is seen to be considerably larger than the 1/e value predicted by the snowplow plus diffusion model. This result is typical. Generally, the measured diameter of the well-exposed photographic image of neutral clouds are considerably larger than would be predicted by the snowplow model.

As we shall see in the next section, the size of the neutral cloud at early time has a considerable impact on the deposition of ions in the ion cloud. We therefore undertook a detailed examination of the photographic image of the Spruce neutral cloud at 20 seconds after release. Technology International Corporation kindly supplied us with a densitometer tracing of a horizontal scan of the Spruce neutral cloud at 20 seconds after release from film record #71715. This film is a color positive film so that the image of the neutral cloud appears light-colored compared to the dark blue sky background.

Figure 2. 5 is a representation of the measured transmittance of the image of the neutral cloud. The image is slightly asymmetric and the dashed vertical line is drawn through the peak transmittance. Also indicated by the short vertical bars and the horizontal arrow is a quantitative representation of the full width of the Spruce neutral cloud that had been previously measured by eye. We see that this measured width corresponds to the outer fringes of the neutral cloud where it begins to have a significant contrast with respect to the background sky. One millimeter on the film plane corresponds to 1. 16 km.

The characteristics of exposed film are usually given by D-log E curves where the optical density $D = \log (1/T)$, T is the transmittance, and E is the energy density ($\mathrm{erg/cm^2}$) incident on the film. Such characteristics are not available for color film in general. We have attempted to extract useful quantitative information regarding the actual distribution of light intensity incident on the film by trying various models of film behavior that produce reasonable D-log E curves. These various analyses produced similar qualitative results and the quantitative differences were not great. As an example, if the number of absorbers remaining in the exposed film decreases exponentially with the number of photons incident, then the density of the film after development is given by $D = D_o \exp(-kI)$ where k and D_o are arbitrary constants. The light intensity incident on the film can be written $I = I_b + I_c(r)$ where I_b is the intensity of the sky background and $I_c(r)$ is the intensity of light from the cloud. The distribution of intensity of the neutral cloud can then be expressed in terms of the transmittance of the image of the neutral cloud as

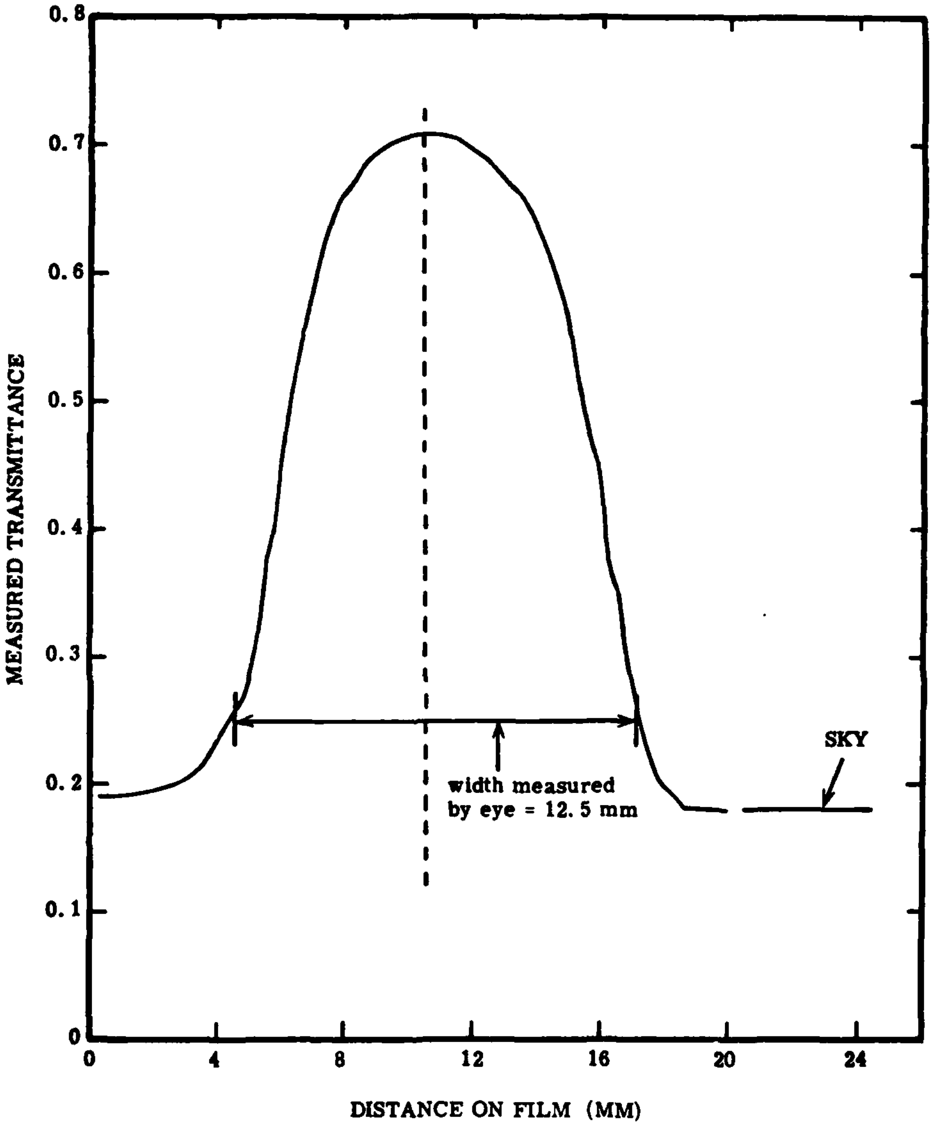

Figure 2.5. Measured transmittance of the Spruce neutral cloud image at 20 seconds after release as recorded on film record #71715. (Original densitometer tracing courtesy of W. Boquist, Technology International Corporation.)

$$I_c(r) = C \log \left[\frac{\log (1/T)}{\log \left(1/T_b\right)} \right] \tag{2.18}$$

where T_b is the transmittance of film background.

The original of Figure 2.5 was used to determine the intensity of the image of the neutral cloud as a function of radius according to Eq. (2.18). Because of the asymmetry in the image of the neutral cloud, three different distributions were determined. One distribution corresponded to the right-half of the cloud, the second corresponded to the left-half of the cloud and the third corresponded to the half-width. For the right-half and left-half of the cloud, the appropriate measured background transmittances, 0.18 and 0.19 respectively, were used. The third determination provided a different distribution than the average of the first two because the right-half value 0.18 was used for the background transmittance. The D-log E film characteristic that results in Eq. (2.18) is consistent with a ratio of $I_c(0)/I_b = 2.5$ which is in agreement with typical measured values of $I_c(0) \sim 0.3$ erg cm^{-2} s^{-1} sr^{-1} and $I_b \sim 0.125$ erg cm^{-2} s^{-1} sr^{-1} at a solar depression angle near 8°.

Figure 2.6 shows a plot of the logarithm of the intensity in arbitrary units as determined above versus the square of the radius for the three different sets of measurements. If the transmittance of the film were related to the intensity in the cloud by Eq. (2.18), and if the intensity distribution in the cloud were Gaussian, the data points would lie on a straight line. We see that for more than an order of magnitude change in intensity beginning at approximately one-half the value of the central intensity, the distribution does appear to be Gaussian.

We have attempted to compare the scale length and the shape determined by these data points with the same quantities determined by the theoretical model developed earlier in this section. With the assumption that the 1/e point is given by Eq. (2.16) and has reached a value of 4.7 km at 20 s after release, and that diffusion was turned on at approximately 2 s after release, we have determined the resulting shapes of the model density distribution for values of τ_D around 0.4 appropriate for 20 s after release. Three such shapes determined by the theoretical model are shown by the three solid curves. The central intensity of each curve was adjusted arbitrarily in order to match the data points at large radius.

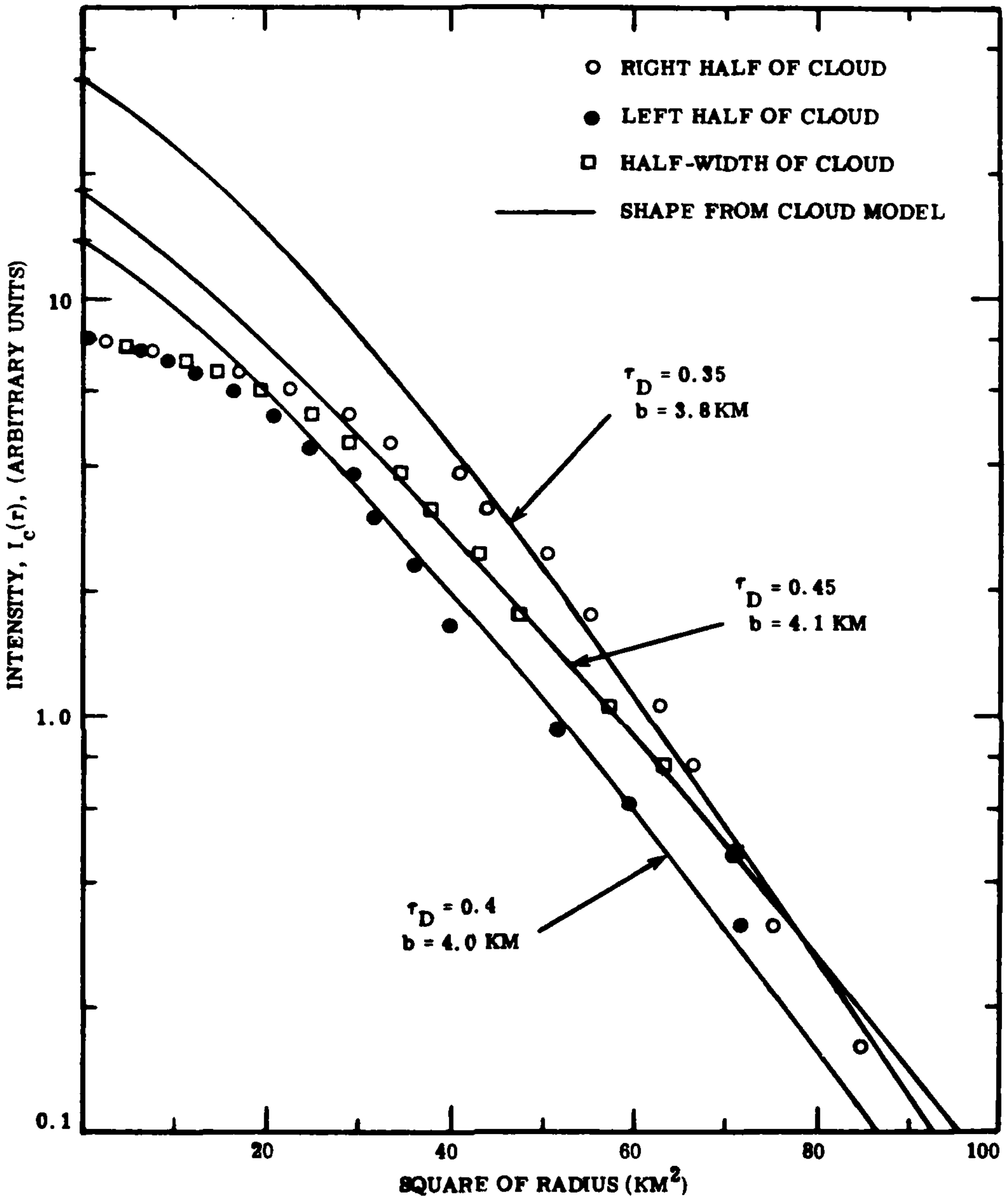

Figure 2.6. Comparison of the measured intensity distribution of the Spruce neutral cloud at 20 seconds after release with the electron density profile determined from a snowplow model with diffusion added.

The comparison of the theoretical model shapes with the shapes determined from the photograph indicates excellent agreement for values of intensity roughly a factor of 2 below the measured peak intensity of the cloud. Two important features of the theoretical curves appear to be consistent with the data. The outer edges of the density profile are fit well by a Gaussian shape, $\exp(-r^2/b^2)$, and the values of the Gaussian scale length, b, (indicated in Figure 2.6) are in agreement. This agreement indicates that a value of the diffusion parameter τ_D of around 0.4 is appropriate. We further note that the scale length 4.7 km determined by the snowplow model as the radius at which the density has fallen to 1/e of its central value is consistent with the observed intensity distributions.

We feel that this analysis provides a plausible explanation for the apparent discrepancy in Figure 2.4 in comparing the measured cloud radius with the results of the theoretical modeling according to snowplow with diffusion added. It is suggested that the dimensions of well-exposed images of neutral clouds during the first few minutes after release (and after the first few seconds) greatly exceed the Gaussian radii of the clouds.

The measured intensity at the center of the ion cloud is somewhat depressed below the theoretical model values. There are three possible factors contributing to this observation. One possibility is that the central portion of the neutral cloud was less peaked at 20 s after release than predicted by the theoretical model. This flatter shape would be consistent with the assumption that the emitted distribution of barium vapor at these low altitudes is more shell-like than the flat-top distribution we have assumed. It is more likely that the derived intensity distribution is not proportional to the actual density distribution within the cloud. First, optical depth effects within the cloud would lead to a flatter intensity distribution than the actual distribution of vapor. Second, Eq. (2.18) may not be reasonable in the highly exposed regions where the film may be approaching saturation. Indeed, a simple modeling of the saturation effect results in a more peaked distribution of the data points in the central region without changing the data points in the outer region significantly. The corresponding best fit value of τ_D would be reduced to 0.3-0.35 which is still within a reasonable range.

3. DEPOSITION OF THE ION CLOUD

In this section we discuss the creation of the ion cloud from the expanding neutral barium atom cloud that was discussed in the previous section. We will describe the procedure for calculating the ion deposition and defer the development of a specific model for Spruce until Section 5.

In this section we are concerned only with the early development of the ion cloud, that is, with the deposition of the ionization which takes place during the first minute following release. In Section 4 we will describe the motion of the ionization and its change in shape along magnetic field lines at times greater than one minute after release. In Section 5 we will put together a unified model for the Spruce ion cloud by combining the procedures developed in this section for the deposition of the ions at early time and the later time behavior of the ion cloud discussed in the next section.

We first give a qualitative description of the deposition process. By about one second after release the neutral barium atom vapor has expanded at essentially constant velocity and approaches a spherical volume with approximately an equal-mass-radius. At this time the concentration of the barium atoms within the neutral cloud is comparable to the ambient local concentration of around 10^{16} particles m^{-3}. Solar radiation excites ground-state barium atoms into metastable states. The population of neutral barium atoms is depleted by two competing processes: photoionization from the excited metastable states and oxidation by ambient oxygen molecules. Haerendel[7] of the Max-Planck Institute has consistently reported photoionization times of order 19 seconds while Best[8] of AFCRL reports a time closer to 30 seconds. In our model we will choose 24 seconds as being within 20% of the correct value. We shall also take the oxidation rate constant of barium by atmospheric O_2 to be 7.5×10^{-11} cm^3/s . The fraction, f , of available barium atoms that are ionized is equal to the ratio of the photoionization rate to the total loss rate of barium atoms due to both photoionization and oxidation,

$$f = \frac{1}{1 + 1.8 \times 10^{-9} N_{O_2}} \quad . \tag{3.1}$$

The time constant, τ_i , for the loss of Ba is

$$\tau_i = 24\,f = \frac{24}{1 + 1.8 \times 10^{-9} N_{O_2}} \quad s \quad . \tag{3.2}$$

For the Spruce cloud released at 190 km, the ionization time constant, τ_i , is equal to 10 seconds.

In the previous section we discussed the expansion of the neutral cloud. We have shown that by including diffusion the neutral cloud quickly evolves towards a Gaussian shape with an equivalent Gaussian radius, R(t) , given by Eq. (2.16). We designate by N_T the total number of barium atoms produced in the release. Since only the fraction f of these atoms become ions, and the time scale on which the neutrals are depleted is τ_i , we find that we can write the source function for the creation of barium ions as

$$S(r,t) = f\,n_b(r,t)/\tau_i = \frac{f N_T}{\tau_i} \; \frac{\exp\left(-r^2/R^2(t)\right)}{\left(\pi R^2(t)\right)^{\frac{3}{2}}} \, e^{-t/\tau_i} \quad . \tag{3.3}$$

where $n_b(r,t)$ is the concentration of barium atoms.

We designate the field line content $\int n dz$ by N(r, t) where r now represents a radius perpendicular to $\vec{B}$, and neglect the transport transverse to the magnetic field during the ion deposition. By integrating the continuity equation (1.1) along magnetic field lines, we can derive the following equation which governs the time and spatial dependence transverse to the magnetic field of the deposition of ions on a field line;

$$\frac{\partial N}{\partial t} = \frac{f N_T}{\tau_i \pi} \frac{\exp\left(-r^2/R^2(t)\right)}{R^2(t)} e^{-\left(t-t_i\right)/\tau_i} . \qquad (3.4)$$

If we start the ionization process at time, t_i, after release we can integrate Eq. (3.4) in order to determine the radial profile of the field-line-content of the ion cloud;

$$N(r,t) = \frac{f N_T}{\tau_i \pi} \int_{t_i}^{t} \frac{\exp\left(-r^2/R^2(t')\right)}{R^2(t')} e^{-\left(t'-t_i\right)/\tau_i} \, dt' . \qquad (3.5)$$

It is appropriate that we delay the start of photoionization until times greater than 1 - 1.5 seconds when the neutral cloud has expanded to an equal-mass-radius. Prior to this time the concentration of barium atoms is so high that optical depth effects prohibit the metastable exciting radiation to permeate the neutral cloud. Indeed, for very large barium releases uniform excitation of the neutral barium atoms might be delayed for several seconds. The barium atom and neutral air densities only approach the nominal ambient values at times longer than it takes $R(t)$ to exceed the equal-mass-radius. On the other hand, radar sensors have shown that the peak ion concentration rises quite rapidly within the first few seconds after release[9] so t_i cannot be taken to be too large.

To exemplify the distribution of ionization on field lines that results from this model we have carried out the necessary integrations to determine the field-line content as a function of radius transverse to the magnetic field. Explicitly, if we define $\bar{a}$ as the size of the Gaussian radius of the neutral cloud at the time $t = t_i + \tau_i$ after release, i.e., at one ionization time constant after ionization has been assumed to begin, we may write the field-line content as;

$$N(r,t) = \frac{f N_T}{\pi \bar{a}^2} I(r,t) \qquad (3.6)$$

where

$$I(r,t) = \frac{\bar{a}^2}{\tau_i} \int_{t_i}^{t} \frac{\exp\left(-r^2/R^2(t')\right)}{R^2(t')} e^{-\left(t'-t_i\right)/\tau_i} \, dt' . \qquad (3.7)$$

$I(r,t)$ represents a normalized field-line content. The normalization is chosen so that

$$\frac{1}{\bar{a}^2} \int_0^{\infty} I(r,t) \, 2 r \, d r = \left[1 - \exp\left(-\left(t - t_i\right)/\tau_i\right)\right] \quad . \qquad (3.8)$$

which approaches one as $t \rightarrow \infty$.

We have carried out the integration indicated in Eq. (3.7) in order to determine the resulting distribution of ions on field lines.

The four thin solid curves in Figure 3.1 show the normalized final (as $t \rightarrow \infty$) field-line content, $I(r,\infty)$, for several different delay times, t_i , before the onset of photoionization. As t_i increases, the radius of the neutral cloud is larger at the time that photoionization begins. As to be expected, the ionization is less peaked at the center and is broader for larger t_i . Note that each of the curves is scaled to the radius, $\bar{a}$, of the neutral cloud at $t = t_i + \tau_i$, thus, the actual spread in kilometers for increasing t_i is greater than indicated.

The heavy curve shows the assumed Gaussian shape of the neutral cloud on the same scale. This is the shape that the ion content would have if all of the ionization were created in a time small compared to the expansion time of the neutral cloud, i.e., as if all of the ionization were deposited instantaneously at $t = t_i + \tau_i$. Figure 3.1 indicates that the scale size of the ion cloud transverse to the magnetic field is considerably narrower than the scale size of the neutral cloud. It is also considerably narrower than that used in the previous modeling.[1] The area under each of the five curves multiplied by $2 r/\bar{a}$ is equal to one indicating that each curve represents the same total inventory of ions.

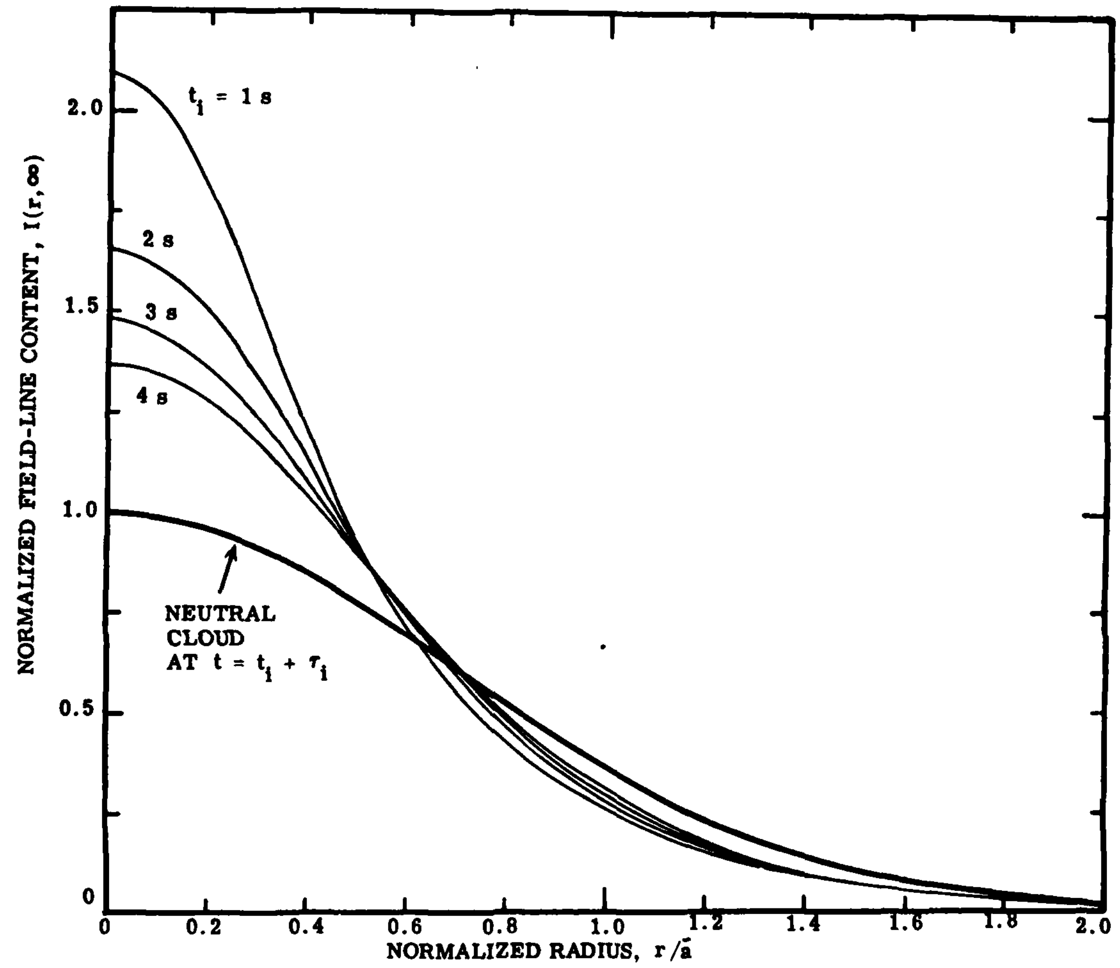

Figure 3.1. Normalized field-line ion content deposited by the expanding neutral cloud as a function of radius transverse to the magnetic field line. Four curves are shown for photoionization beginning at four different times, t_i , after release.

We will make use of this ion deposition model in order to derive parameters appropriate for the Spruce ion cloud in Section 5. We will mention here that the total field line content at the center of the ion cloud according to model A is $2.4 \times 10^{17} m^{-2}$.

4. MOTION AND DESCENT OF THE ION CLOUD

In this section we discuss the motion of the ion cloud in the vertical direction and derive the distribution of ionization in the ion cloud along magnetic field lines. We find that the simple but useful model described here allows us to obtain the rate at which the ion cloud settles under the influence of gravity and neutral winds, and the change in shape of the distribution of ionization parallel to the magnetic field. We find that the ion cloud evolves into a characteristic shape rather quickly and maintains this shape as it descends through the upper atmosphere. The model includes the response of the ion cloud to the force of gravity, spreading of ionization along the magnetic field lines due to ambipolar diffusion, and the flattening of the bottom side of the ion cloud as it descends into the denser neutral atmosphere.

From this model we determine the peak electron density in the ion cloud as a function of time as well as describe the change in the characteristic width of the peak of the electron density.* Furthermore, we shall calculate the change in the Pedersen conductivity of the ion cloud as it descends. Lastly, we shall compare the results of the analytic solution obtained here with the results of the numerical solution obtained by Chavin and Kilb.[10]

The deformations that take place in the ion cloud contours in the plane perpendicular to the magnetic field will not be discussed in this section. These deformations, ultimately resulting in the development of striations, have been the subject of other analytical and numerical studies. Neither will we be concerned here with the factors that lead to stabilization of short wavelengths or mechanisms that control the diffusion of the plasma cloud perpendicular to the magnetic field.

---

*Electron concentration and ion concentration are equal to each other and will be used interchangeably throughout this report. Electron density or ion density is sometimes used to mean the same quantity.

4.1 BASIC MODEL AND EQUATIONS

For our model we adopt a number of simplifying assumptions. We assume that the ions and electrons are isothermal with temperatures T_i and T_e respectively. We take the magnetic field, $\vec{B}$, as uniform and constant but making a dip angle, θ, with the horizontal direction. We assume that the number density of the neutral atmosphere, n_n, varies exponentially with height, h, with a constant scale height, H_n, i.e., $n_n = n_{no} \exp\left(-(h-h_o)/H_n\right)$. We also assume that the electrons are completely collisionless, undergoing no collisions with either neutrals or ions.

We adopt a coordinate system oriented with the magnetic field which we take to be pointing downward and northward. Positive x will be towards the east. The z-direction is anti-parallel to $\vec{B}$ and positive y points toward the north and upwards. The acceleration due to gravity, $\vec{g}$, is vertically downwards and has components $g_z = -g \sin\theta$ and $g_y = -g\cos\theta$.

By setting S in Eq. (1.1) equal to 0, we write the ion continuity equation as

$$\frac{\partial n}{\partial t} + \nabla_\perp \cdot n\vec{v}_{i\perp} + \frac{\partial}{\partial z} n v_{iz} = 0 \tag{4.1}$$

where n is the plasma density and the ion velocity $\vec{v}_i$ is given explicitly in terms of components anti-parallel to $\vec{B}$ and perpendicular to $\vec{B}$. The equations of motion for the ions and the electrons are

$$0 = e\left(\vec{E} + \vec{v}_i \times \vec{B}\right) - T_i \nabla \ln(n) - \nu M\left(\vec{v}_i - \vec{v}_n\right) + M\vec{g}, \tag{4.2a}$$

$$0 = -e\left(\vec{E} + \vec{v}_e \times \vec{B}\right) - T_e \nabla \ln(n), \tag{4.2b}$$

where $\vec{E}$ is the electrostatic field, $\vec{v}_n$ is the neutral wind velocity, M is the ion mass, ν is the ion-neutral collision frequency, and the temperatures are given in energy units. We have neglected the inertial terms because the development of the cloud takes place on a time scale typically measured in minutes which is long compared to the collision time $\tau = 1/\nu$ which has typical values of 0.1 - 2.0 s depending on altitude. Our model treats the electrons as being completely collisionless and massless.

It is convenient to explicitly separate the ambipolar part of the electrostatic field, $\left(T_e \nabla \ln(n)\right)/e$, from the remaining part, $\vec{E}'$, which remains constant along a magnetic field line (as we shall see below). Thus, we write the electrostatic field as

$$\vec{E} = \vec{E}' - \frac{T_e}{e} \nabla \ln(n) \, . \tag{4.3}$$

Note that since $\nabla \times \vec{E} = 0$, we also have $\nabla \times \vec{E}' = 0$. If we define $\vec{u} \equiv \vec{v}_n + \vec{g}\tau$, we may rewrite the ion and electron momentum equations as

$$0 = e\left(\vec{E}' + \vec{v}_i \times \vec{B}\right) - 2T \nabla \ln(n) - \nu M\left(\vec{v}_i - \vec{u}\right) \, , \tag{4.4a}$$

$$0 = -e\left(\vec{E}' + \vec{v}_e \times \vec{B}\right) \, , \tag{4.4b}$$

where we have defined T as equal to the average of the ion and electron temperatures, $T = \left(T_i + T_e\right)/2$. In this form we can see that the effect of gravity on the ion cloud is indestinguishable from the effect of a neutral wind with velocity $\vec{g}\tau$. Although Perkins et al.[11] state that gravity acts like an electric field in the potential equation, it actually appears precisely as a neutral wind because it creates a body force on the plasma in the same manner that collisions with neutrals do and exerts no force on the electrons as an electric field would.

The force equation on the plasma cloud is obtained by adding Eqs. (4.4a & b) resulting in

$$\vec{j} \times \vec{B} = \nabla p + \nu n M\left(\vec{v}_i - \vec{u}\right) \tag{4.5}$$

where $\vec{j} = en\left(\vec{v}_i - \vec{v}_e\right)$ is the current density and $p = n\left(T_i + T_e\right)$ is the total plasma pressure. In this form we see that the current flowing perpendicular to the magnetic field consists of two parts: a diagmagnetic part that provides pressure balance transverse to the magnetic field and the remaining part that overcomes the drag between the ions and the neutrals (and the force of gravity). It is the latter part that determines the slip velocity transverse to the magnetic field that produces the deformations of the ion cloud leading to backside steepening and striation formation, subjects not discussed here.

The component of Eq. (4.5) parallel to the magnetic field gives the parallel ion velocity

$$v_{iz} = u_z - \frac{2T}{\nu M}\frac{\partial}{\partial z}\ln(n) . \qquad (4.6)$$

The component of Eq. (4.4b) parallel to the magnetic field shows that $E_z' = 0$. This fact together with the fact that $\vec{E}'$ is curl-free, $\nabla \times \vec{E}' = 0$, shows that $\vec{E}'$ has components only perpendicular to the magnetic field and these components are functions only of the coordinates transverse to the magnetic field independent of z. (Remember that z does not measure distance in the vertical direction but distance along the magnetic field line.)

In order to obtain the ion velocity perpendicular to the magnetic field from Eq. (4.4a) it is convenient to introduce the vector $\vec{F}$ which has only components perpendicular to the magnetic field

$$\vec{F} = \frac{\vec{E}'}{B} + \vec{u} \times \hat{b} - \frac{2T}{eB}\nabla_{\perp}\ln(n) \qquad (4.7)$$

where $\hat{b} = \vec{B}/B\left(= -\hat{e}_z\right)$ is the unit vector in the direction of the magnetic field. By defining ϵ as the ratio of the ion-neutral collision frequency to the ion gyrofrequency, Ω,

$$\epsilon = \frac{\nu M}{eB} \equiv \frac{1}{\Omega\tau} , \qquad (4.8)$$

we may represent the solution of Eq. (4.4a) for the perpendicular component of the ion velocity as

$$\vec{v}_{\perp i} = \vec{u}_{\perp} + \frac{1}{1+\epsilon^2}\left(\vec{F} \times \hat{b} + \epsilon\, \vec{F}\right)$$

$$= \vec{v}_{\perp o} + \frac{\epsilon}{1+\epsilon^2}\left(\vec{F} - \epsilon\, \vec{F} \times \hat{b}\right) , \tag{4.9}$$

where

$$\vec{v}_{\perp o} = \frac{\vec{E}' \times \vec{B}}{B^2} - \frac{2T}{eB}\, \nabla \ln(n) \times \hat{b}$$

$$= \frac{\vec{E} \times \vec{B}}{B^2} - \frac{T_i}{eB}\, \nabla \ln(n) \times \hat{b} \quad . \tag{4.10}$$

At high altitudes, above 140 km, the parameter $\epsilon \ll 1$. To lowest order in ϵ the ion drift velocity is given by $v_{\perp o}$. By recognizing that $\nabla \cdot \nabla n \times \hat{b} = 0$ and $\nabla \times \vec{E}' = 0$, the continuity equation for the ions, Eq. (4.1), can be rewritten as

$$\frac{\partial n}{\partial t} + \frac{\vec{E}' \times \vec{B}}{B^2} \cdot \nabla_{\perp} n + \frac{\partial}{\partial z}\left(n\, u_z - \frac{2T}{\nu M}\frac{\partial n}{\partial z}\right) = 0 \quad . \tag{4.11}$$

We thus see that in lowest order the perpendicular motion of the ion cloud corresponds to incompressable flow transverse to the magnetic field.

The equation that determines $\vec{F}$ and thus the electrostatic field $\vec{E}'$ from Eq. (4.7) is obtained by first setting $\nabla \cdot \vec{j} = e\nabla \cdot n\left(\vec{v}_i - \vec{v}_e\right) = 0$ which can be written

$$\nabla_{\perp} \cdot \frac{\epsilon}{1+\epsilon^2}\, n\, \vec{F} = \nabla_{\perp} \cdot \frac{\epsilon^2}{1+\epsilon^2}\, n\, \vec{F} \times \hat{b} - \frac{1}{e}\frac{\partial}{\partial z} j_z \quad . \tag{4.12}$$

The first term on the right-hand-side represents the divergence of the Hall contribution to the current which is less than the Pedersen current given on the left-hand-side. An approximate equation for $\vec{E}'$ which depends only on coordinates transverse to the magnetic field is obtained by integrating Eq. (4.12) along the magnetic field line and neglecting the Hall contribution to the current which is higher order in ϵ . Even if the region of integration extends to low altitude where $\epsilon \geqslant 1$, this approximation is still valid if the field-line-integrated Hall current is much less than the Pedersen current. Although this approximation is not valid during the daytime or in the auroral zone during auroral precipitation, it is valid after sunset at midlatitudes. The pressure contribution to $\vec{F}$ is relatively small so for simplicity we neglect this term for the moment. This neglect has no essential impact on the arguments which follow.

By carrying out the integration of Eq. (4.12) parallel to $\vec{B}$ with the above approximations, and making the usual assumption that no current flows out of the ionosphere along magnetic field lines, the equation for $\vec{E}'$ can be simply written

$$\nabla_{\perp} \cdot \Sigma(x, y) [\vec{E}' + \vec{U} \times \vec{B}] = 0 \ . \qquad (4.13)$$

Σ is the field-line-integrated Pedersen conductivity and $\vec{U}$ is a field-line-weighted average of the velocity field, $\vec{u}_{\perp}$, defined by

$$\Sigma\left(x, y; z_c\right) = \frac{e}{B} \int \frac{\epsilon n}{1 + \epsilon^2} \, dz \ , \qquad (4.14)$$

$$\vec{U}\left(x, y; z_c\right) = \frac{\int \frac{\epsilon n}{1 + \epsilon^2} \vec{u}_{\perp} \, dz}{\int \frac{\epsilon n}{1 + \epsilon^2} \, dz} \qquad (4.15)$$

Note that although Σ and $\vec{U}$ are explicit functions of the transverse coordinates, they are also functionals of the distribution of ionization along the magnetic field and thus of the z-coordinate of the center of the cloud, z_c. Note that if $\vec{u}_\perp = \vec{v}_{n\perp} + \vec{g}\tau$ where $\vec{v}_{n\perp}$ = constant and if we define

$$\bar{\nu}\left(x, y; z_c\right) = \frac{\int \frac{\nu n}{1+\epsilon^2} dz}{\int \frac{n}{1+\epsilon^2} dz}$$

then

$$\vec{U} = \vec{v}_{n\perp} + \frac{g \cos\theta}{\bar{\nu}} .$$

The set of equations (4.11), (4.13), (4.14) and (4.15) is the fundamental set that controls the motion of plasma clouds in the ionosphere. This set is equivalent to the standard equations used by other workers.[11, 12, 13, 14] The principle approximations made are: (1) the neglect of electron collisions whose principal influence is to cause $\vec{E}'$ to have a slight variation along the magnetic field; and (2) the neglect of Hall current and other terms of higher order in ϵ. Neither of these effects has an influence on either the motion of ionization along the magnetic field or on the zeroth order motion transverse to the field that are the subjects of discussion in the following subsections. The importance of these neglected effects on striation behavior and the amount of sophistication of treatment needed to incorporate them is an unsettled question and an area of active investigation beyond the scope of this report.

These equations do incorporate additional features not ordinarily included that do have a bearing on the subject of the behavior and motion of the ion cloud. They include a neutral atmosphere whose density is a function of altitude and a neutral wind velocity field that is not spatially uniform. The effect of gravity is included and has been shown to have the same effect as a downward neutral wind whose magnitude is inversely proportional to the neutral density. In the next subsection we discuss the motion of the ion cloud that results from these equations.

4.2 MOTION OF THE ION CLOUD

The qualitative properties of the solution of Eq. (4.13) are well known. For small plasma clouds that make a very small change in the Pedersen conductivity, Σ, the quantity in brackets is essentially constant and $\vec{E}'$ has essentially the value of the ambient electric field $\vec{E}_a$. On the other hand, high-density plasma clouds that cause significant change in the field-line-integrated Pedersen conductivity causes the term in brackets to be nearly zero for those magnetic field lines that pass through the center of the ion cloud. Thus $\vec{E}'$ for those field-lines has the approximate value $-\vec{U} \times \vec{B}$.

We may derive useful approximate expressions for the velocity of the center of the ion cloud transverse to the magnetic field line by separately identifying the ambient ionospheric density n^a and the ion cloud density n^c. For the field line that passes through the center of the cloud at the coordinates $x = x_c$ and $y = y_c$, we write

$$\Sigma\left(x_c, y_c; z_c\right) = \Sigma^a + \Sigma^c , \tag{4.16}$$

where Σ^c is the field-line-integrated Pedersen conductivity of the cloud, and Σ^a the field-line-integrated Pedersen conductivity of the ionosphere. The velocity of the center of the ion cloud transverse to the magnetic field, $\vec{V}_{c\perp}$, can be written

$$\vec{V}_{c\perp} = \frac{\vec{E}'\left(x_c, y_c; z_c\right) \times \vec{B}}{B^2} = \eta \vec{U}\left(x_c, y_c; z_c\right) + (1 - \eta) \frac{\vec{E}_a \times \vec{B}}{B^2} \tag{4.17}$$

where η is the coupling coefficient of the ion cloud to the field-line-weighted neutral wind $\vec{U}$. η is a function of Σ^c/Σ^a that has the following properties:

$$\eta\left(\frac{\Sigma^c}{\Sigma^a}\right) \sim \begin{cases} 0 ; & \Sigma^c << \Sigma^a \\ 1 ; & \Sigma^c >> \Sigma^a \end{cases} . \tag{4.18}$$

Note that this definition of a coupling parameter differs from previous descriptions in terms of the parameter $\zeta = 1 - \eta$.

If we further define

$$\vec{U}_a = \frac{\displaystyle\int \frac{\epsilon n^a}{1+\epsilon^2}\, \vec{u}_\perp \, dz}{\displaystyle\int \frac{\epsilon n^a}{1+\epsilon^2}\, dz} ,$$

$$\alpha = \frac{\Sigma^c}{\Sigma^a} ,$$

$$\vec{u}_{\perp c} = \vec{u}_\perp \left(x_c, y_c; z_c\right) ,$$

then we may define $\vec{U}_c$ as having the approximate value

$$\vec{U}_c \equiv \vec{U}\left(x_c, y_c; z_c\right) \sim \frac{\vec{U}_a + \alpha \vec{u}_{\perp c}}{1+\alpha} = \vec{U}_a + \frac{\alpha}{1+\alpha}\left(\vec{u}_{\perp c} - \vec{U}_a\right) . \qquad (4.19)$$

For a cylindrically symmetric model ion cloud with a constant density inside a finite radius and zero density outside, $\eta(\alpha)$ has the following functional form,[14]

$$\eta(\alpha) = \alpha/(2+\alpha) . \qquad (4.20)$$

Other studies of the influence of shape on the motion of ion clouds[15, 16] have shown that this approximation to $\eta(\alpha)$ slightly over-estimates the actual amount of coupling to the neutral wind for ion clouds with more realistic transverse density profiles. However, in terms of $\eta(\alpha)$ given by Eq. (4.20), we may write an explicit expression for the velocity of an ion cloud transverse to the magnetic field;

$$\vec{V}_{c\perp} = \frac{\alpha \vec{U}_a + \alpha^2 \vec{u}_{\perp c}}{(1+\alpha)(2+\alpha)} + \frac{2}{2+\alpha} \frac{\vec{E}_a \times \vec{B}}{B^2} \tag{4.21}$$

This expression should be approximately valid throughout the range $0 \leq \alpha \leq \infty$. In the appropriate limits it says that low-density clouds $(\alpha << 1)$ move perpendicular to $\vec{B}$ with the ambient $\vec{E}_a \times \vec{B}/B^2$ velocity while high-density clouds $(\alpha >> 1)$ are carried along with the neutral wind at the location of the cloud.

The motion parallel to the magnetic field is precisely $u_{zc} = u_z(x_c, y_c; z_c)$. Hence the motion of the cloud is obtained by combining the perpendicular and parallel motions. For instance, we will derive expressions for the downward motion of an ion cloud in the earth frame in terms of the northward, v_N , and downward, v_D , components of the neutral wind. Eastward components of the neutral wind do not affect vertical motion of ion clouds. Since

$$\vec{u}_\perp = \left[v_N \sin\theta - (v_D + g\tau)\cos\theta\right] \hat{e}_y \tag{4.22}$$

and denoting the y-component of $\vec{U}(x_c, y_c; z_c)$, (see Eq. (4.15)) by U_c , and by using Eq. (4.17), we may write the downward component of velocity of an ion cloud as

$$V_{cD} = -\eta U_c \cos\theta + \left[(v_D + g\tau)\sin\theta + v_N\cos\theta\right]\sin\theta + (1-\eta)\frac{E_w}{B}\cos\theta \tag{4.23}$$

where E_w is the westward component of the ambient electric field.

For low-density clouds, the downward velocity is obtained by setting $\eta = 0$ in Eq. (4.23) which can be written

$$V_{cD} \sim u_z \sin\theta + \frac{E_w}{B}\cos\theta \tag{4.24}$$

i.e., the cloud motion is simply the component of $\vec{u}$ parallel to $\vec{B}$ plus the $\vec{E} \times \vec{B}$ motion transverse to $\vec{B}$. A low-density cloud slides up and down the field lines in response to the neutral forces parallel to $\vec{B}$ and crosses field lines according to $\vec{E} \times \vec{B}$ motion. Thus northward and downward neutral winds, gravity, and westward electric fields all contribute to downward motion of low-density clouds.

For high-density clouds, $\eta = 1$ and U_c is the y-component of $\vec{u}_\perp$ given by Eq. (4.22). The expression (4.23) reduces to

$$V_{cD} \sim v_D + g\tau \qquad (4.25)$$

i.e., the ion cloud descends as though there were no electric and magnetic fields present. One word of caution must be raised at this point. Although high-density ion clouds move as though there were no magnetic and electric field present, it must not be assumed that the ionization behaves as though it were uncharged. If Eq. (4.11) is integrated parallel to the magnetic field, the resulting equation shows that the total field-line-integrated ionization content is a conserved quantity. Every piece of ionization on a given field line moves across magnetic field lines at the same velocity even in the limit of high-density clouds.

4.3 VERTICAL DISTRIBUTION OF IONIZATION

We now turn our attention to determining the vertical motion of the ion cloud and its change of shape along the magnetic field line. We shall restrict ourselves to the special but reasonable case that the neutral wind field depends only on altitude

$$h - h_o = y \cos \theta + z \sin \theta \qquad (4.26)$$

where h_o is the initial altitude of the cloud and the origin of the x, y, z coordinate system is at the initial location of the center of the cloud. The altitude of the center of the cloud, $h_c(t)$, can be calculated as a function of time,

$$t = -\int_{h_o}^{h_c} \frac{dh}{V_{cD}(h)} \quad , \tag{4.27}$$

where V_{cD} is the altitude-dependent downward velocity. The velocity of the ion cloud in the y-direction, $V_{cy}(h_c(t))$, as given by combining Eqs. (4.22) and (4.19) with (4.17), is now an explicit function of t which can be integrated to obtain the y-coordinate of the field line passing through the center of the ion cloud,

$$y_c(t) = \int_0^t V_{cy}\left(h_c(t')\right) dt' \quad . \tag{4.28}$$

We will now show that the changes in density that occur along nonvertical magnetic field lines for a particular class of altitude-dependent neutral winds can be described by an equation valid for vertical magnetic fields and no neutral wind. The distribution of ionization along the central magnetic field line is given by the function

$$n_c(z, t) = n\left(x_c, y_c, z, t\right) \quad , \tag{4.29}$$

where x_c and y_c are the coordinates of the field line passing through the center of the cloud. The equation for $n_c(z, t)$ is obtained by transforming Eq. (4.11) to the frame of reference that is moving with the cloud velocity $\vec{V}_c$ given by Eq. (4.17) transverse to the magnetic field. This transformation allows us to write the ion continuity equation in the form

$$\frac{\partial n_c}{\partial t} + \frac{\partial}{\partial z}\left(n_c u_{zc} - \frac{2T}{\nu_c M} \frac{\partial n_c}{\partial z}\right) = 0 \tag{4.30}$$

where u_{zc} and ν_c are functions of the altitude along the field line passing through the center of the cloud,

$$h = h_o + y_c(t)\cos\theta + z\sin\theta \ . \qquad (4.31)$$

The ion-neutral collision frequency is proportional to the atmospheric density which we will assume varies exponentially with a constant atmospheric scale-height, H_n ,

$$\nu = \nu_o \exp\left(-\left(h - h_o\right)/H_n\right) \ . \qquad (4.32)$$

Furthermore, we assume that the component of $\vec{u}$ along the magnetic field has the explicit altitude dependence

$$u_z = -U_{z1} - U_{z2}\exp\left(\left(h - h_o\right)/H_n\right) \ . \qquad (4.33)$$

U_{z1} is a constant downward drift parallel to the magnetic field while the second term corresponds to a constant downward flux of neutral particles. We also take the transverse component of the ion cloud velocity to have the same form;

$$V_{cy} = -V_{y1} - V_{y2}\exp\left(\left(h - h_o\right)/H_n\right) \ . \qquad (4.34)$$

With the definitions $V_{D1} = V_{y1}\cos\theta + U_{z1}\sin\theta$ and $V_{D2} = V_{y2}\cos\theta + U_{z2}\sin\theta$, the downward velocity of the center of the cloud has the same form,

$$V_{cD} = V_{D1} + V_{D2}\exp\left(\left(h - h_o\right)/H_n\right) \qquad (4.35)$$

We may now explicitly carry out the integrations given in Eqs. (4.27) and (4.28) which yield

$$\begin{aligned} h_c(t) - h_o &= -V_{D1}t - H_n \ln\left[1 + \frac{V_{D2}}{V_{D1}}\left(1 - \exp\left(-V_{D1}t/H_n\right)\right)\right] \\ &= -H_n \ln\left[\left(1 + \frac{V_{D2}}{V_{D1}}\right)\exp\left(V_{D1}t/H_n\right) - \frac{V_{D2}}{V_{D1}}\right] ; \qquad (4.36) \end{aligned}$$

$$y_c(t) = -V_{y1}t - \frac{V_{y2}H_n}{V_{D2}} \ln\left[1 + \frac{V_{D2}}{V_{D1}}\left(1 - \exp\left(-V_{D1}t/H_n\right)\right)\right] \quad (4.37)$$

Note that for times longer than it takes to drift a scale-height, H_n/V_{D1}, the cloud descends at constant velocity, V_{D1}, and has covered a distance only $H_n \ln(1 + V_{D2}/V_{D1})$ greater than the distance $V_{D2}t$. If there is no vertical constant drift, $V_{D1} = 0$, then Eq. (4.36) reduces to

$$h_c(t) - h_o = -H_n \ln\left(1 + V_{D2}t/H_n\right) \quad . \quad (4.38)$$

Note that in this case, the downward velocity

$$-\frac{dh_c(t)}{dt} = \frac{V_{D2}}{1 + \frac{V_{D2}}{H_n}t} \quad (4.39)$$

at first is V_{D2} as to be expected but decreases only as t^{-1} and not exponentially at late time.

We now introduce a new coordinate $z' = z + U_{z1}t$ and transform Eq. (4.30) to a frame drifting down the magnetic field line with speed U_{z1}. Set $n_c(z, t) = \tilde{n}(z', t)$, and obtain

$$\frac{\partial \tilde{n}}{\partial t} = \frac{\partial}{\partial z'}\left[\exp\left(-d^*(t) + \frac{z' \sin\theta}{H_n}\right)\left(U_{z2}\tilde{n} + D_o\frac{\partial \tilde{n}}{\partial z'}\right)\right] \quad (4.40)$$

where $D_o = 2T/\nu_o M$ and

$$d^*(t) = \frac{U_{z1}t\sin\theta - y_c(t)\cos\theta}{H_n}$$

$$= \frac{V_{D1}t}{H_n} + \frac{V_{y2}\cos\theta}{V_{D2}} \ln\left[1 + \frac{V_{D2}}{V_{D1}}\left(1 - \exp\left(-V_{D1}t/H_n\right)\right)\right] .$$

(4.41)

$d^*(t)$ is the vertical distance downward measured in scale-height units H_n that the cloud has moved due to the constant drift U_{z1} along field lines plus the transverse motion across field lines. Equation (4.40) describes the evolution of the ion cloud. If $U_{z2} = 0$ and $\sin\theta = 0$ corresponding to horizontal magnetic field lines, it describes diffusion of the cloud with a time-dependent diffusion coefficient as the cloud drifts downward across field lines. If $U_{z2} \neq 0$, there is also a time-dependent drift along field lines which does not influence the change in shape. If $\sin\theta \neq 0$, the effective diffusion coefficient is also a function of position along the field-line.

Equation (4.40) can be brought into the simple form

$$\frac{\partial n^*}{\partial t^*} = \frac{\partial}{\partial z^*}\left[e^{z^*}\left(\frac{\partial n^*}{\partial z^*} + a n^*\right)\right] \tag{4.42}$$

where $z^* = z' \sin\theta/H_n$, $\tilde{n}(z', t) = n^*(z^*, t^*)$, $a = U_{z2} H_n/D_o \sin\theta$ and

$$t^* = \frac{D_o \sin^2\theta}{H_n^2}\int_o^t e^{-d^*(t')}\,dt'$$

$$= \frac{1}{a}\left\{\left[1 + \frac{V_{D2}}{V_{D1}}\left(1 - \exp\left(-V_{D1} t/H_n\right)\right)\right]^{U_{z2}\sin\theta/V_{D2}} - 1\right\}. \tag{4.43}$$

$n^*(z^*, t^*)$ gives the density distribution as a function of altitude measured in scale height units H_n. As $t \to 0$, $t^* \to D_o t \sin^2\theta/H_n^2$ and as $t \to \infty$, $t^* \to$ constant unless $V_{D1} = 0$. If gravity alone acts to pull particles down field lines, then $U_{z2} = g\sin\theta/\nu_o$ and we can write

$$a = \frac{g H_n}{\nu_o D_o} = \frac{H_n}{H_c} = \frac{T_n M}{\left(T_e + T_i\right) M_n} \tag{4.44}$$

where H_c is the barium plasma scale height, T_n and M_n are the atmospheric temperature and the mean molecular weight. For electrons only a little hotter than ions and molecular weights around 20, a has a value around 3.

Equation (4.42) describes the descent of neutral particles in an exponential atmosphere and its solution was given by Yu and Klein[17] in the form

$$n^*(z^*, t^*) = \frac{C}{t^*} \xi^{a+1} \exp\left[- \frac{1 + \xi^2}{t^*} \right] I_{a-1} \left(\frac{2\xi}{t^*} \right) \qquad (4.45)$$

where $\xi = \exp(- z^*/2)$ and I_{a-1} is the modified Bessel function of order a-1 . The normalization constant is determined by integrating the cloud density along the field line and designating the maximum total field line content of the cloud by N_c ,

$$N_c = \int_{-\infty}^{\infty} \tilde{n}(z', t) \, dz' = \frac{H_n}{\sin \theta} \int_{-\infty}^{\infty} n^*(z^*, t^*) \, dz^* = \frac{H_n}{\sin \theta} C \qquad (4.46)$$

so that $C = \dfrac{N_c \sin \theta}{H_n}$.

At early and late times, the approximations to the Bessel function valid for large and small values, respectively, of its argument[18] can be applied to give the behavior of the density at early and late times:

$$\begin{aligned} n(z^*, t^*) &\sim \frac{N_c \sin \theta}{H_n \sqrt{4\pi t^*}} \exp\left(- \frac{z^{*2}}{4t^*} \right), \quad z^*, t^* \ll 1 , \\ &= \frac{N_c}{\sqrt{4\pi D_o t}} \exp\left(- \frac{z'^2}{4 D_o t} \right), \quad t \to 0 ; \end{aligned} \qquad (4.47)$$

$$n(z^*, t^*) \sim \frac{N_c \sin\theta}{H_n \Gamma(a)} \left(\frac{\xi^2}{t^*}\right)^a \exp\left(-\frac{\xi^2+1}{t^*}\right)\left[1 + O\left(\frac{\xi^2}{a t^{*2}}\right)\right], \quad t^* >> \xi$$

$$\sim \frac{N_c \sin\theta}{H_n \Gamma(a)} a^a e^{-a} \left(\frac{\xi^2}{\xi_m^2}\right)^a \exp\left(-a\left(\frac{\xi^2}{\xi_m^2} - 1\right)\right)\left[1 + O\left(\frac{1}{t^*}\right)\right]; \qquad (4.48)$$

where for the sceond expression $t^* >> 1$ and the maximum value occurs at $\xi^2 = \xi_m^2 = a t^*$. At early time, the solution given by Eq. (4.47) corresponds to diffusion of a point release in a constant density atmosphere and hence is applicable to barium releases from about a minute after release after the ion deposition phase discussed in the preceeding section has finished.

The asymptotic form valid at late time given by Eq. (4.48) can be compared to another exact solution of Eq. (4.42), $\bar{n}$, which is valid for all values of t^* but satisfies an initial condition different from that satisfied by Eq. (4.45);

$$\bar{n}(z^*, t^*) = \frac{N_c \sin\theta}{H_n \Gamma(a)} \left(\frac{a\xi^2}{1 + a t^*}\right)^a \exp\left(-\frac{a\xi^2}{1 + a t^*}\right)$$

$$= \frac{N_c \sin\theta}{H_n \Gamma(a)} a^a e^{-a} \left(\frac{\xi^2}{\xi_m^{*2}}\right)^a \exp\left[-a\left(\frac{\xi^2}{\xi_m^{*2}} - 1\right)\right]$$

$$\cong \frac{N_c \sin\theta}{H_n} \sqrt{\frac{a}{2\pi}} \exp\left(-a\left(z^* - z_m^*\right) - a\left[\exp\left(-\left(z^* - z_m^*\right)\right) - 1\right]\right)$$

$$(4.49)$$

where

$$\xi_m^{*2} \equiv e^{-z_m^*} = 1 + a t^* \qquad (4.50)$$

is the value of ξ^2 at which $\bar{n}$ reaches its maximum value. The only approximation in the last expression is in using Stirling's formula[18] for $\Gamma(a)$. By using Eq. (4.43) for t^* and recognizing that

$$d^*(t) - z_m^*(t) = \left(h_o - h_c(t)\right)/H_n \quad , \tag{4.51}$$

we can write the solution $\bar{n}$ as an explicit function of altitude

$$\bar{n}(z^*, t) = \frac{N_c \sin\theta}{H_n} \sqrt{\frac{a}{2\pi}} \exp\left(- a\left[\frac{h - h_c(t)}{H_n} + \exp\left(- \frac{h - h_c(t)}{H_n}\right) - 1\right]\right). \tag{4.52}$$

The solution $\bar{n}$ corresponds to a density distribution of constant shape with its maximum at $h = h_c(t)$ given by Eq. (4.36). Near the peak, the density has a Gaussian shape,

$$\bar{n}\left(h \rightarrow h_c , t\right) \sim \frac{N_c \sin\theta}{\sqrt{2\pi H_n^2/a}} \exp - \frac{\left(h - h_c(t)\right)^2}{2 H_n^2/a} \tag{4.53}$$

but decays exponentially, $\bar{n} \sim \exp\left(-\left(h - h_c\right) a/H_n\right)$, at high altitude with a scale-height H_n/a . It decays more rapidly than a Gaussian fall-off on the lower side.

The density distribution given by $\bar{n}$ in Eq. (4.49) is identical to that given by the asymptotic distribution in Eq. (4.48) to order $1/t^*$. The location of the peak given by $\xi_m^{*2} = 1 + at^*$ is accurate but not exact and has the correct values for both small and large t^* . Numerical evaluation shows that the shape of $n(z^*, t)$ is well approximated by $\bar{n}(z^*, t)$ for $at^* \geq 2$.

The shape $\bar{n}$ is the same as that discussed by Rao[19] in connection with barium clouds for the case $U_{z2} = g\tau \sin\theta$ and no neutral winds. We have derived the fully time-dependent solution for the density distribution including altitude-dependent winds and magnetic field of arbitrary dip. Before giving examples for specific cases we make some general observations.

The factors that influence the shape of the density distribution are the values of t^* and

$$U_{z2} = -v_{z2} + g\tau \sin\theta \ ,$$

that is, gravity and an altitude-dependent component of the neutral wind parallel to the magnetic field. The value of t^* is strongly influenced by the downward displacement, d^*, of the cloud. If d^* is small, an underestimate of the time, t_a, it takes the cloud to evolve to the asymptotic shape given by $\bar{n}$ is obtained by setting the early-time Gaussian width (see Eq. (4.47)) equal to the asymptotic value $(2 H_n^2/a \sin^2\theta)^{\frac{1}{2}}$. This procedure results in $t_a \sim H_n^2/2 a D_o \sin^2\theta$ which is equivalent to (see Eq. (4.43)) $a t^* \sim 0.5$ or about 1/4 of the time indicated by numerical evaluation. After $4 t_a$, the electron density in the vicinity of the peak is proportional to $(U_{z2}/g \tau \sin\theta)^{\frac{1}{2}}$ and the Gaussian scale length along the magnetic field is $H' = (2 H_n H_c g\tau/U_{z2} \sin\theta)^{\frac{1}{2}}$.

However, downward motion of the cloud transverse to the magnetic field and a constant drift parallel to the magnetic field each have a strong influence on the time development of the cloud. If $V_{D1} = 0$, no constant downward drift of the cloud but only altitude-dependent downward drift across field lines, then it takes longer than $4t_a$ to reach the asymptotic shape $\bar{n}$. If there is a constant downward drift, $V_{D1} \neq 0$, then inspection of Eq. (4.43) shows that t^* approaches a constant value, t_f^*. Generally $a t_f^* \sim 1$ but if $V_{D1} >> U_{z2}$, the value of $a t_f^*$ can be much less than 1. In this case of rapid descent of the ion cloud, its final shape would remain Gaussian-like with a narrower, higher-valued peak than that predicted by $\bar{n}$.

4.4 DENSITY PROFILES FOR SPECIFIC CASES

The effect of the neutral wind on the time development of an ion cloud is discussed here for several specific cases. In particular, we show the effects due to altitude-dependent and altitude-independent neutral winds, downward and upward neutral winds, and the response of both small and large barium releases.

The formulas derived in the last subsection depend on an atmospheric density model in which the ion-neutral collision frequency varies exponentially with altitude according to Eq. (4.32). An expression for the collision time, $\tau = 1/\nu$, can be obtained from measurements of the mobility of barium ions in nitrogen gas[20] resulting in

$$\tau = \frac{8.6 \times 10^{15}}{\bar{n}_n} \text{ s} \tag{4.54}$$

where $\bar{n}_n$ is an effective neutral concentration in particles/m^3 ,

$$\bar{n}_n = n_{N_2} + n_{O_2} + 0.8\, n_O \quad . \tag{4.55}$$

In deriving Eq. (4.54) it has been assumed that the collision cross section varies inversely as the square root of the temperature and that the collision cross section for oxygen molecules and atoms is the same as it is for nitrogen molecules. The fact that the lighter oxygen atoms are less efficient in stopping a heavier barium ion is expressed by the appropriate Langevin factor,

$$\left(1 + M_{Ba}/M_{N_2}\right)^{\frac{1}{2}} \left(1 + M_{Ba}/M_O\right)^{-\frac{1}{2}} \sim 0.8 \quad ,$$

where M_{N_2} and M_O are the masses of the nitrogen molecule and oxygen atom respectively.

In order that a comparison of the results of our analytic calculations can be made with the numerical values obtained by Chavin and Kilb[10] when they did a simulation of event Anne, we have used their atmospheric density model. The solid curve in Figure 4.1 shows the effective density, $\bar{n}$, obtained using their values. The dashed line shows an exponential fit to the height variation of the effective density resulting in an effective scale height of 22 km. This scale height is somewhat less than the atmospheric density scale height because the concentration of oxygen atoms, which are dominant above 150 kilometers altitude, increases less rapidly than the mass density at lower altitudes as a result of chemical reactions. By combining the above numbers we obtain the desired expression for the altitude-dependence of the product $g\tau$,

$$g\tau = g\tau_0 \exp\left((h - 180)/22\right) \qquad (4.56)$$

where $g\tau_0 = 7.7$ m/s .

General expressions for the ion cloud velocity perpendicular to the magnetic field and downward are given by Eqs. (4.21) and (4.23), respectively. If $\vec{u}$ and $\vec{V}_{c\perp}$ have an altitude-dependence in the forms given by Eqs. (4.33) and (4.34), we find that the general form for the downward motion of the ion cloud, Eq. (4.23), also has the form assumed in Eq. (4.35). For the specific cases of low-density and high-density clouds, the downward velocities reduce to the simple expressions given in Eqs. (4.24) and (4.25), respectively and are expressable in the form given by Eq. (4.35). Note particularly that for low-density clouds, the presence of a westward component of the ambient electric field has the same effect as a constant downward neutral wind. The westward directed electric field gives rise predominantly to a southward electric field drift as well as to a small downward component.

Table 4.1 provides a listing of the parameters used in order to illustrate the effects of different vertical neutral winds. All clouds start out initially with a Gaussian shape drifting with an appropriate constant velocity. It is only at late times that the effect of different neutral winds becomes apparent. Case 1 corresponds to no neutral wind with the ion cloud just settling under the influence of gravity alone. Cases 2, 3 and 4 provide examples of

Table 4.1. Cases illustrated.

Case No.	Cloud Size	Downward Neutral Wind (m/s)	Southward Electric Field Drift (m/s)	$\frac{V_{D1}}{g \tau_o}$	$\frac{V_{D2}}{g \tau_o}$	a	Time After Release (hours)	Fig. No.
1a	Large	0	Arbitrary	0	1.0	3	1.5	4.3-4.6
1b	"	"	"	"	"	"	0.25	4.3
1c	"	"	"	"	"	"	0.75	4.3
1d	"	"	"	"	"	"	3.0	4.3
2	"	+5.2E[a]	"	0	1.67	5	1.5	4.4
3	"	+5.2C[b]	"	0.67	1.0	3	1.5	4.4
4	"	+20C	"	2.6	1.0	3	0.5	4.4
5a	"	-5.2E	"	0	0.33	1	1.5	4.5
5b	"	"	"	"	"	"	4.5	4.5
6	"	-5.2C	"	-0.67	1.0	3	1.5	4.5
7	Small	0	0	0	0.75	3	1.5	4.6
8	"	+5.2E	0	0	1.25	5	1.5	4.6
9	"	0	10.4C	0.67	0.75	3	1.5	4.6

[a] The symbol E represents exponential variation with altitude, $E \sim \exp((h - 180)/22)$

[b] The symbol C represents a constant, uniform drift.

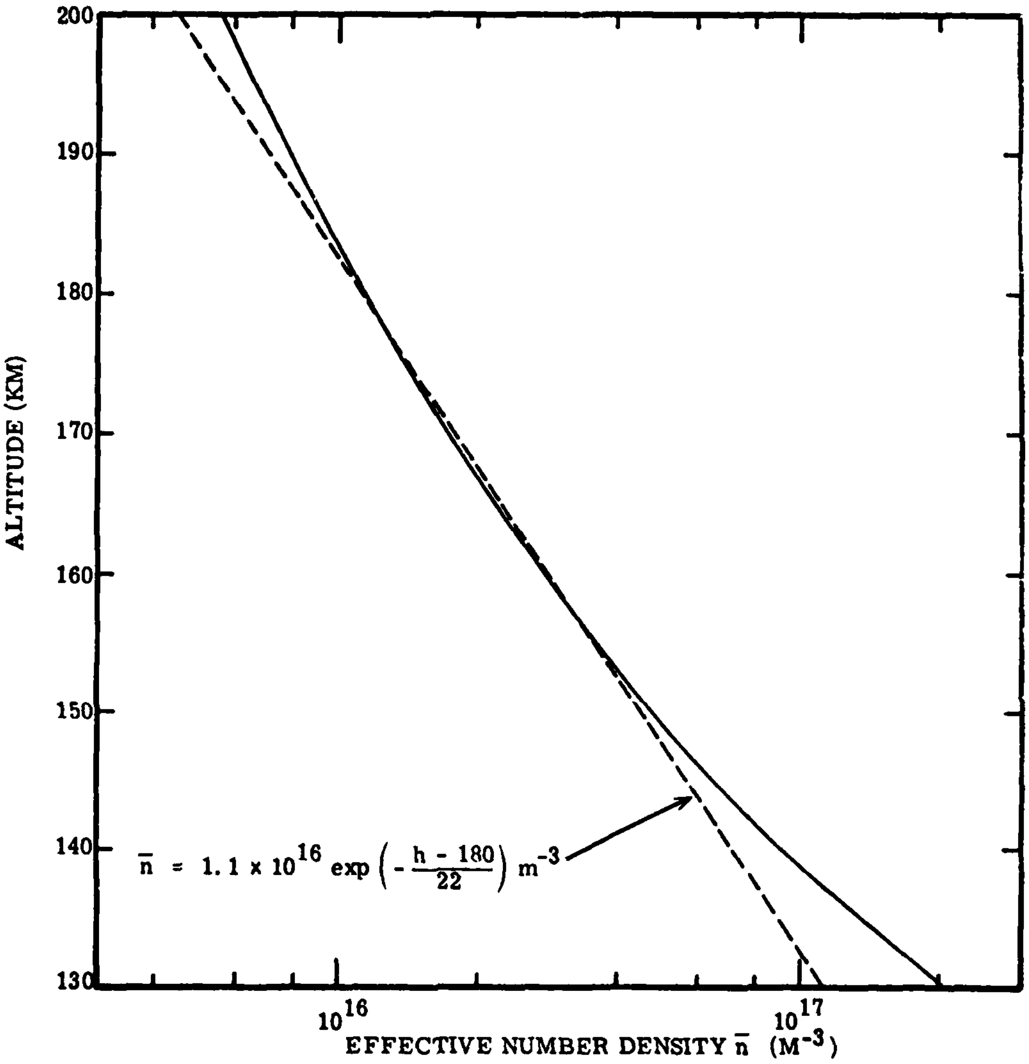

Figure 4.1. The effective number density vs. altitude derived from the atmospheric density model used by Chavin and Kilb. The solid curve shows the calculated values and the dashed curve shows the exponential fit to the model that is a good approximation between 150 and 185 kilometers altitude.

different downward neutral winds. In Case 2 the velocity is assumed to vary exponentially with the form given by Eq. (4.35). Cases 3 and 4 correspond to moderate and large downward constant neutral winds. The resulting values of V_{D1}, V_{D2} and a (defined after Eq. (4.42)) for these cases are given in the fifth, sixth and seventh columns, respectively, of Table 4.1.

Cases 5 and 6 correspond to upward neutral winds increasing exponentially in the former case and remaining constant in the latter but with the same magnitudes as in Cases 2 and 3. For comparison, Cases 7, 8 and 9 correspond to the motion of small ion clouds where the nonvertical magnetic field inhibits the downward motion of the cloud. The specific values are chosen to correspond to Cases 1, 2 and 3 respectively. We note that the electric field does not influence the motion of large ion clouds which move with the neutral wind. An electric field in a nonvertical magnetic field, however, has an equivalent effect on a small ion cloud that a constant neutral wind has on a large ion cloud.

The expression (4.36) for the altitude of the center of the ion cloud has been evaluated for each of the 9 cases. The results are shown in Figure 4.2. In Case 2 the cloud behaves as though there were an effective gravity 1.67 g. The cloud reaches the same altitude as in case 1 in three-fifths of the time. Cases 3 and 4 show the obvious result that a large downward constant wind is more effective in bringing the cloud to lower altitudes. Case 5 corresponds to an exponentially varying upward neutral wind producing motion equivalent to a value of gravity equal to 0.33 g. It reaches the same altitude as the cloud in Case 1 in a time three times as long. In the case of a constant upward neutral wind as in Case 6, the peak density in the cloud moves to an altitude at which $g\tau$ is equal to the upward velocity. Cases 7, 8 and 9 show that a small ion cloud does not descend quite as rapidly as the corresponding large clouds shown in Cases 1, 2 and 3. In general, the peak density in the ion cloud will not rise to an altitude higher than the release altitude unless the upward neutral wind has a value greater than $g\tau_0$ at the altitude of release.

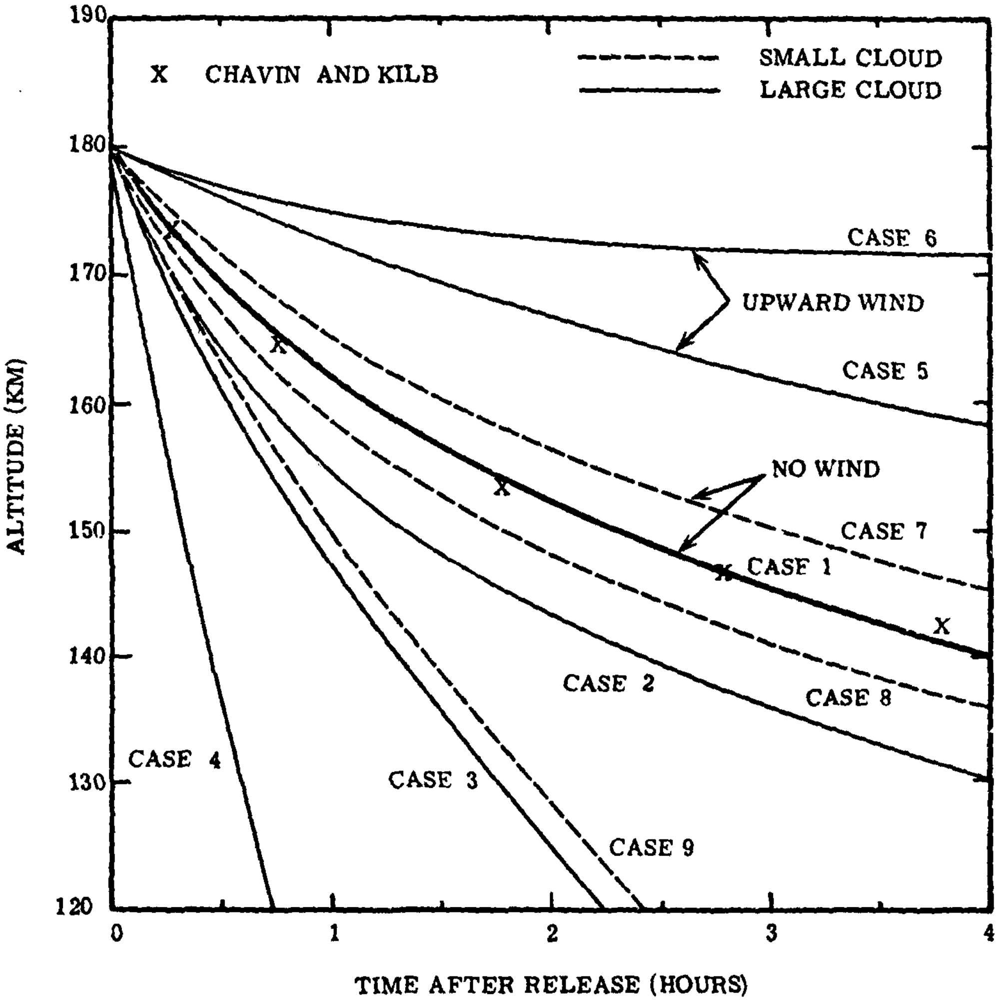

Figure 4.2. Altitude of the peak electron density vs. time for the 9 cases defined in Table 4.1. The five curves below the heavy curve, Case 1, correspond to various downward winds.

The altitudes of the peak electron density obtained by Chavin and Kilb[10] in their numerical simulation of Event Anne are shown plotted by X in Figure 4.2. In their calculations they made the equivalent assumptions of a large ion cloud and no electric fields or neutral winds. The agreement with the Case 1 curve shows that Eq. (4.36) is an appropriate description of the time-dependence of the altitude. Subsequent computer runs by Chavin and Kilb in which horizontal neutral winds were included showed that they had no effect on either the altitude or density profile of the ion cloud which is consistent with the results for large ion clouds as discussed in subsection 4.2.

We now turn our attention to a discussion of the shape of the electron density distribution as a function of altitude. The next to last column of Table 4.1 lists the lapse time since release for the cases illustrated in the figures listed in the last column. Figure 4.3 shows the time development of a large barium cloud under the influence of gravity alone, Case 1. The settling due to gravity and the approach to the asymptotic shape given by Eq. (4.52) is apparent. The density distribution at 1.5 hours after release, Case 1a, is shown with a bold line as this curve will be repeated in the subsequent figures when we compare it to conditions of various neutral winds. The time lapse of 1.5 hours since release corresponds to $t \sim 3\, t_a$ and the bold curve is only slightly narrower with a 5% larger peak density than the asymptotic shape shown at $t = 3$ hours.

We have compared the shapes of the density profiles obtained from the analytic function given in Eq. (4.45) and shown in Figure 4.3 with the results of the density profiles obtained by Chavin and Kilb[10] at corresponding times. Because their initial cloud had a far higher electron content than our cloud which has a content of $2.4 \times 10^{17}\ m^{-2}$, we have arbitrarily rescaled their profiles to have comparable ion content. In general their profiles are broader than the analytic shapes as they employed a more realistic atmospheric model with a value of $H_c = H_n/a$ that was 20% larger than the value we employed for illustrative purposes.

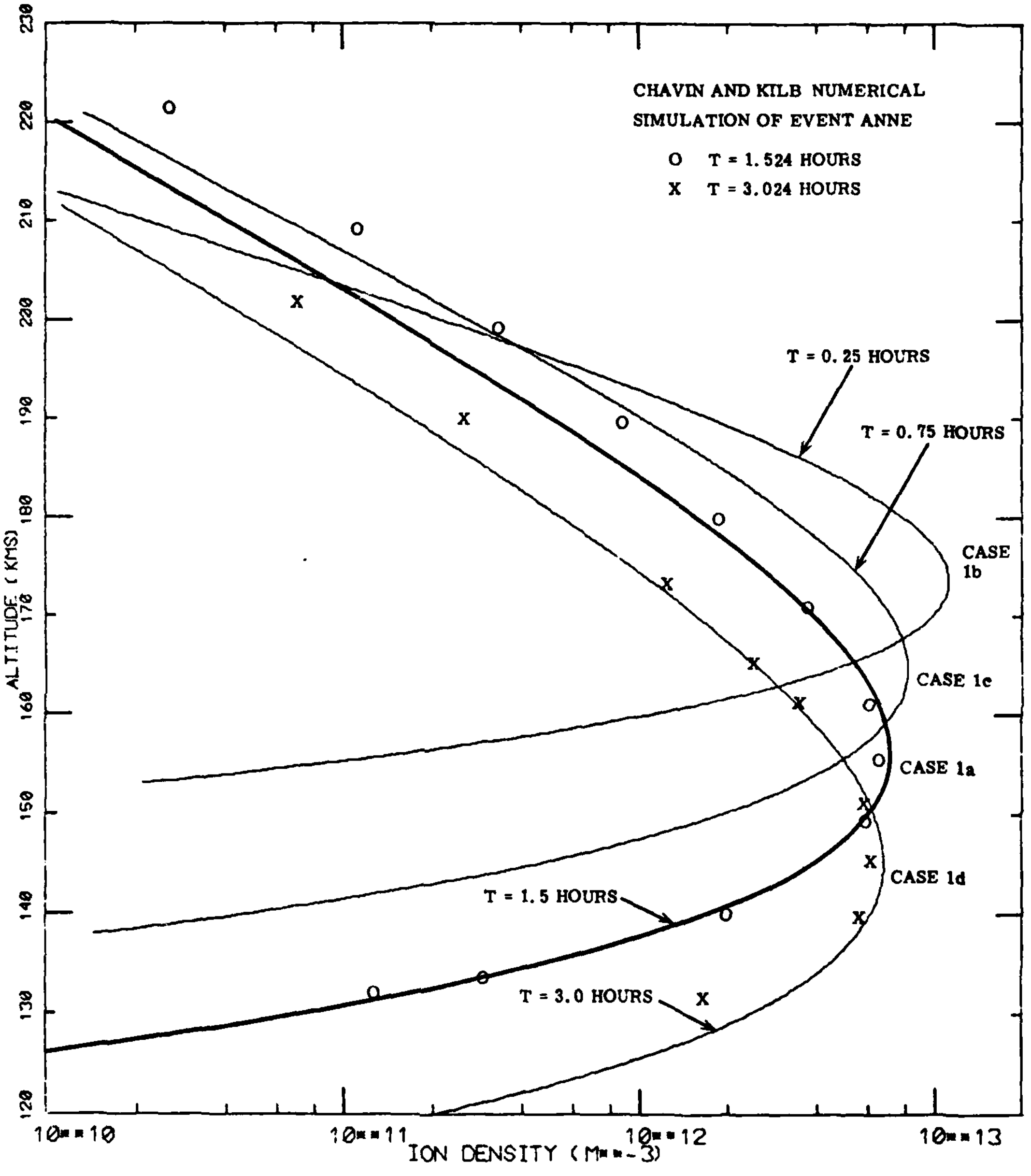

Figure 4.3. Electron density profiles as a function of time in Case 1 of no neutral wind. The cloud descends under the influence of gravity starting from an initial Gaussian shape at 180 kilometers and evolves to the asymptotic shape given by the lowest curve. The data points shown are from the numerical calculations of the simulation of the Event Anne by Chavin and Kilb.

Simulation results for the two later times are shown by O and X respectively. Their larger value of H_c results in their less rapid fall-off of density on the high altitude side. It also contributes to the lowering of the peak electron density although the precise fit in that region is arbitrary. The flattening on the bottom side is due in part to the decreasing scale height in their atmospheric model (see Figure 4.1) and in part results from boundary effects due to the approach to their low altitude limit. The excellent agreement between the analytic curves and the numerical computation indicates that both are giving equivalent descriptions of the physics that was assumed to govern the descent of the ion cloud.

Figure 4.4 shows the effect of downward winds on the density profile of an ion cloud. The heavy curve is Case 1a from the previous figure in which no wind has been acting and the cloud has been settling under gravity alone. Case 2 corresponds to an altitude-dependent downward wind with a magnitude of $0.67\, g\tau_0$ at the altitude of release. The cloud descends to a lower altitude and its asymptotic shape is narrower with a higher peak density. Cases 3 and 4 correspond to constant downward winds of different magnitude shown at different times since release. Note that in Case 3 the ion cloud has arrived at a lower altitude than the cloud in Case 4 even though the product of the constant wind velocity times time is only 3/4 as great as in Case 4. The reason is that in Case 4 the ion cloud descended so rapidly that the settling due to gravity rapidly became ineffective.

The reason for including Case 4 is to illustrate the effect that a larger downward wind has on the asymptotic shape. The asymptotic shape shown by Case 4 ($t^* \sim 0.8\, t_f^*$) is considerably different from that given by the approximate shape $\bar{n}$ in Eq. (4.49). The downward motion has brought the ion cloud into a region of dense atmosphere such that the diffusion coefficient is too small to allow the cloud to diffuse to the equilibrium shape. If the downward neutral wind were to cease then the ion cloud shown in Case 4 would expand and its peak density would be lowered and its density profile would assume the shape that Case 1a has but it would take longer than 1.5 hours.

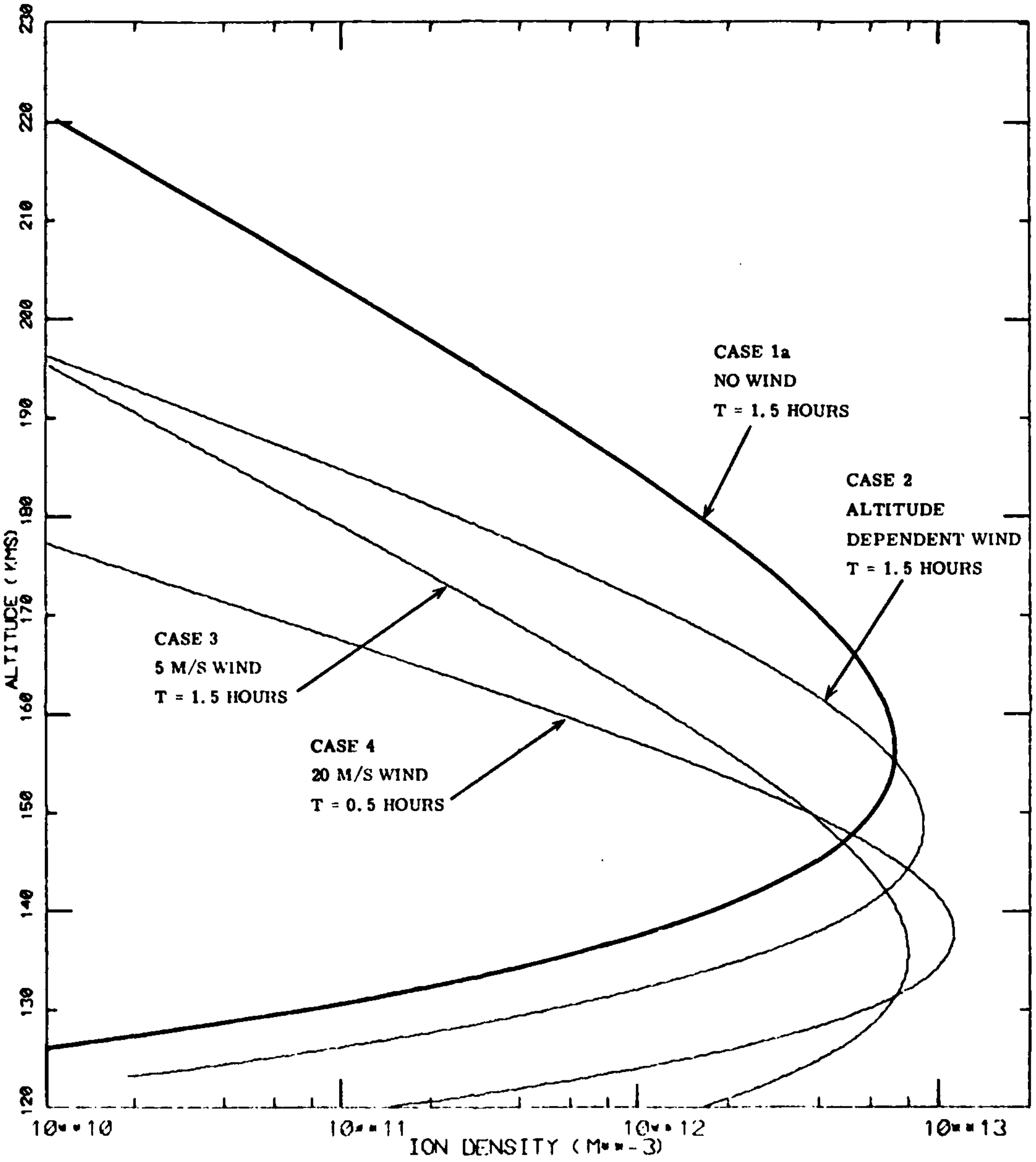

Figure 4.4. Density profiles for various downward neutral winds.

Figure 4.5 shows the effect of upward neutral winds. In Case 5 the altitude-dependent neutral wind has reduced the effective gravity to a value of 0.33 g. The result is a broader, lower-valued peak that descends slowly in altitude. Case 5 is shown for two different times. The earlier time corresponds to Case 1a while at the later time (three times longer) the peak density has been lowered to the same altitude as the peak density in Case 1a. Case 6 corresponds to a constant upward neutral wind. Since the diffusion coefficient at higher altitude is larger, this cloud has already achieved the asymptotic form that Case 1a has almost approached. Note that although these upward winds were too small to raise the peak electron density above the release altitude, they do transport significant ionization to higher altitude.

Figure 4.6 shows the profiles obtained by low-conductivity ion clouds under the influence of downward winds. Cases 7, 8 and 9 correspond to Cases 1a, 2 and 3 for large ion clouds. In each case the shapes of the low-density clouds are comparable to the high-density clouds but they have not descended to quite as low an altitude. This retardation in descent is due to the nonvertical magnetic field. The differences in altitude would of course be much larger for magnetic fields with a dip angle smaller than 60°.

4.5 DISCUSSION

The analysis carried out in this section has been motivated by several issues that arose as a result of the Stress Test Series. The primary questions that were raised were: How quickly can ion clouds descend to low altitudes? Can the peak electron density increase at late time or as the cloud descends in altitude? Can the bulk of the ionization be confined to a narrow altitude range? In considering the answers to these questions, it became apparent that the neutral winds and E × B drifts would have an appreciable effect on the vertical transport of the ion cloud.

We have presented in this section an analytical analysis of the effect of neutral winds on the vertical transport of ionization. Analysis has included the effect of a nonvertical magnetic field and is applicable to ion clouds

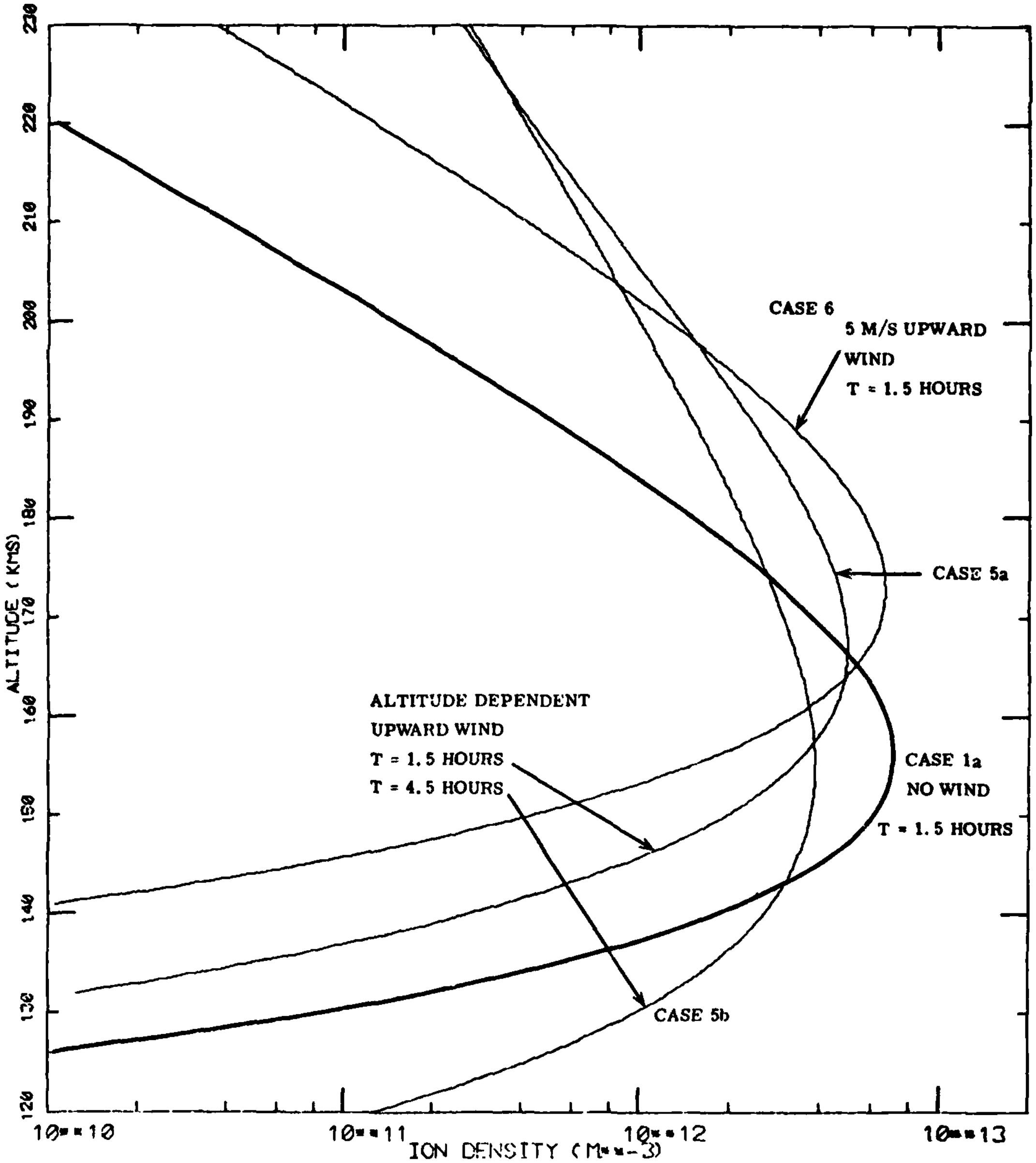

Figure 4.5. Density profiles for various upward neutral winds.

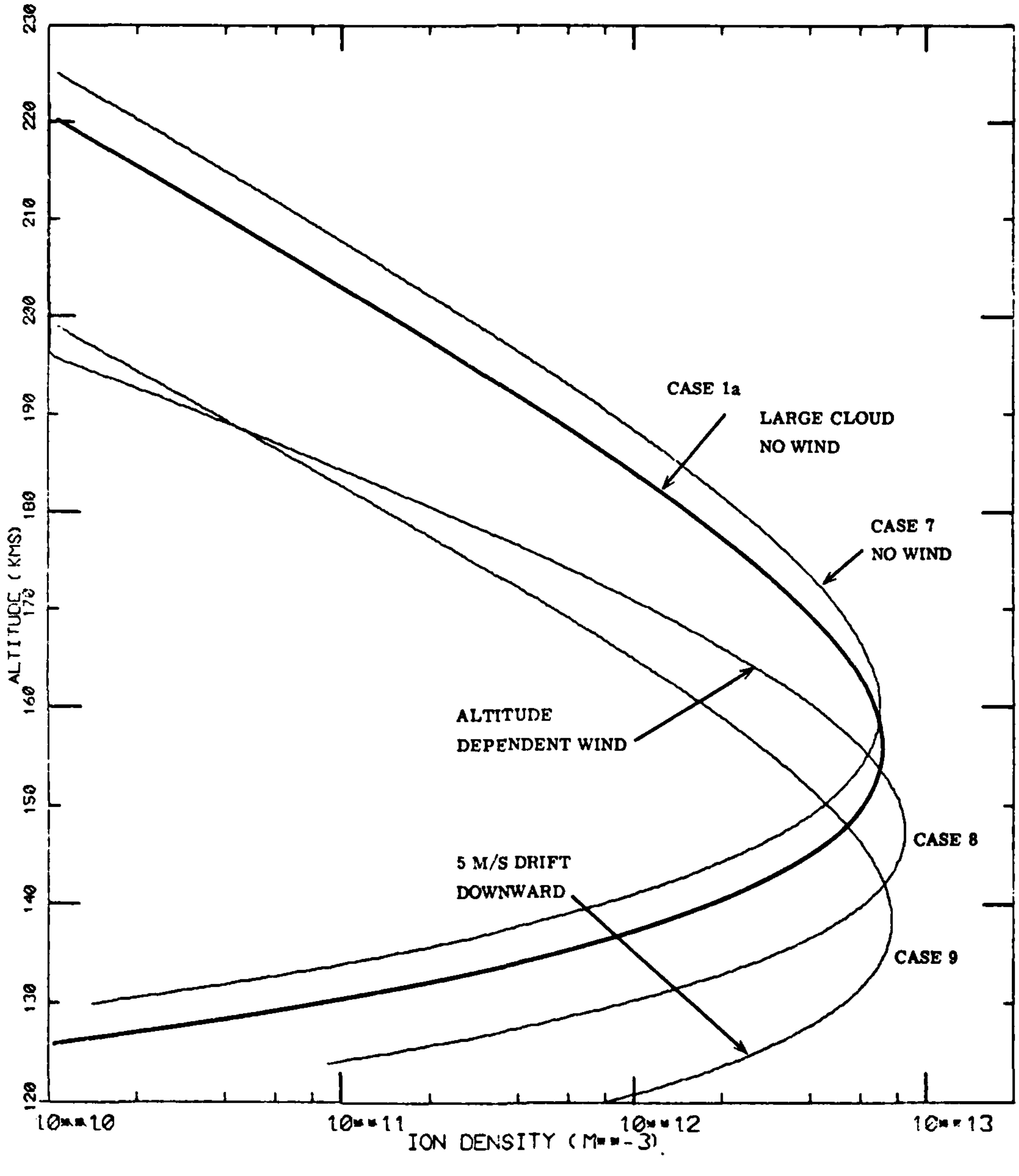

Figure 4.6. Density profiles for low-conductivity ion clouds all at 1.5 hours after release. For comparison purposes the ion content in the low-conductivity clouds was kept at 2.4×10^{17} m^{-2}. Cases 7, 8 and 9 are comparable to Cases 1a, 2 and 3 shown in Figure 4.4.

of arbitrary density. Specific examples for the limits of small and large ion clouds have been illustrated. The comparison of the analytic results obtained here with the numerical results obtained by Chavin and Kilb[10] shows that these different procedures produce similar results. The analytic results have allowed us to investigate the influence of different winds.

We have found that for times of order hours the ion cloud can descend to quite low altitudes with only moderate downward neutral winds. We have found that the peak electron density can remain high and narrow in altitude only if there is a rapid downward drift. Under the conditions of a scale height which is independent of altitude and winds which are constant in time, the peak electron density steadily decreases to its asymptotic value and never increases. However, in a realistic atmosphere in which the temperatures and the mean molecular weight are lower at lower altitudes, the scale height decreases at lower altitudes. The peak electron density can then be expected to increase inversely with the effective number density scale height.

Altitude-independent but time-varying neutral winds do not have a significant effect on the peak electron density. The ion cloud just evolves to the asymptotic form that is appropriate for that altitude. The rate at which the cloud approaches the asymptotic form depends on the altitude at which the ion cloud finds itself. An altitude-dependent neutral wind, on the other hand, can cause changes in the peak electron concentration. An altitude-dependent wind at lower altitudes, say around 150 km, will have a greater effect on the peak electron density than a wind of the same magnitude at a higher altitude. The change in the peak electron density would be gradual and not sudden for reasonable models of the neutral wind. We should note that even in Case 4 for a large downward wind that produced the highest peak electron density and narrowest profile, the full-width at half-max was 15 km in altitude.

A nonvertical magnetic field influences the behavior of small ion clouds more than large ion clouds. However, the examples we have shown indicate that for large dip angles and vertical neutral winds, there is little difference in the behavior of small, low-conductivity ion clouds compared to high-conductivity ion clouds. They settle under the influence of gravity almost as rapidly and achieve essentially identical shapes. The primary difference between low-density and high-density ion clouds is the effect that electric fields and northward neutral winds have on the vertical motion of the ion clouds. As indicated in Eq. (4.23) both westward electric fields and northward neutral winds cause descent of the ion cloud but this effect is less pronounced for high-density ion clouds.

As the cloud changes altitude, the field-line-integrated Pedersen conductivity of the cloud, an important parameter for determining its motion and striation behavior, changes. For our constant scale-height atmospheric model and times when the cloud remains at sufficiently high altitude so that $\epsilon = \nu M/eB << 1$, we can determine the time-dependence of the conductivity explicitly. By neglecting the ϵ^2 in the denominator in Eq. (4.14), making use of Eq. (4.32) for ν, and denoting the initial value of the conductivity when the cloud is confined to an altitude range small compared to H_n by Σ_o, we may write the time-dependent conductivity as

$$
\begin{aligned}
\Sigma(t) &= \frac{\Sigma_o}{N_c} \int_{-\infty}^{\infty} n(z,t) \exp\left(-\left(h-h_o\right)/H_n\right) dz \\
&= \frac{\Sigma_o H_n}{N_c \sin\theta} \int_{-\infty}^{\infty} e^{d^*(t)}\, n^*(z^*, t^*(t))\, e^{-z^*}\, dz^* \\
&= \frac{\Sigma_o H_n}{N_c \sin\theta}\, e^{d^*(t)} \int_{0}^{\infty} 2\xi\, n^*(z^*, t^*)\, d\xi \\
&= \Sigma_o\, e^{d^*(t)} (1 + a t^*) \\
&= \Sigma_o \exp\left(h_o - h_c(t)\right)
\end{aligned}
$$

$$= \Sigma_o \left[1 + \frac{V_{D2}}{V_{D1}}\left(1 - \exp\left(-\frac{V_{D1}t}{H_n}\right)\right)\right] \exp\left(\frac{V_{D1}t}{H_n}\right)$$

$$= \Sigma_o \left[1 + \frac{V_{D2}t}{H_n}\right] \quad \text{if } V_{D1} = 0 \ . \qquad (4.57)$$

In deriving the above, we have made use of the definitions given in Eqs. (4.36), (4.41), (4.42), (4.43), (4.45), (4.46), (4.50) and (4.51) and the evaluation[18]

$$2\int_0^\infty \xi^{\nu+3} \exp\left(-\frac{\xi^2}{t^*}\right) I_\nu\left(\frac{2\xi}{t^*}\right) d\xi = t^*\left[1 + (\nu+1)t^*\right] \exp\left(\frac{1}{t^*}\right) \ .$$

This remarkable result indicates that as the ion cloud is evolving and descending, its Pedersen conductivity is given solely by the value of the altitude of the center of the ion cloud. If there is a constant downward drift, the Pedersen conductivity increases exponentially. If there is no constant downward drift, the Pedersen conductivity increases linearly with time. For the values of the parameters chosen here, appropriate for the Anne cloud, the doubling time for the conductivity is approximately 3/4 of an hour.

5. SPRUCE ION CLOUD MODEL

In Section 2 we provided a description of the expansion of the neutral barium atom vapor cloud. In Section 3 we described the deposition of ionization on magnetic field lines resulting from the photoionization of barium atoms in the expanding neutral cloud. In Section 4 we have discussed factors that influenced the peak electron density* and scale size of the ion cloud parallel to the magnetic field at late times.

We have applied the procedures developed in those sections to obtain models of the Spruce ion cloud. We will first list the parameters, both input and derived, associated with each of three different models, A, B and C. Models A and B differ only in their late-time properties. Model C, on the other hand, provides what we believe to be an underestimate of the total ion inventory in the Spruce ion cloud. We believe that the characteristics of the Spruce ion cloud are best exemplified by the parameters given in model A (or B). Model C is presented as an alternative in order to demonstrate the sensitivity of the models to some of the input assumptions.

Table 5.1 provides a listing of the parameters associated with each of the three models. An examination of the first ten items indicates that the input parameters at early time for models A and B are identical. Examination of the next four input parameters indicate that model A and B differ only in the late-time parameters. Models A and C have identical late-time input parameters.

The most significant input parameter is item 5, the total ion inventory. Model A results from the attempt to maximize the total ion inventory and still have consistency with other reasonable assumptions and maintain reasonable agreement between the derived parameters and interpretations of observations. This value is approximately one-half of the inventory assumed in our previous modeling.[1] This reduction is consistent

---

*See footnote on page 8.

Table 5.1. Parameters for Spruce cloud models

Parameter	(Units)	Model A	Model B	Model C
Inputs to Model - early time (<100s)				
1. Mass of barium vapor, M_o,	(kg)	3.56	3.56	2.46
2. Vaporization efficiency		7.4%	7.4%	5.1%
3. Ionization time constant, τ_i,	(s)	10	10	10
4. Fraction of atoms ionized, f,		0.42	0.42	0.42
5. Total ion inventory	(10^{24})	6.5	6.5	4.5
6. Atmospheric density, ρ_a,	(kg/km^3)	0.45	0.45	0.45
7. Neutral diffusion coefficient, D_n,	(km^2/s)	0.052	0.052	0.052
8. Equal mass radius, a_o,	(km)	1.26	1.26	1.09
9. Initial expansion velocity, $\dot{R}_o$,	(km/s)	1.15	1.15	1.20
10. Onset of photoionization, t_i,	(s)	2.0	2.0	1.5
Inputs to Model - late time (>100s)				
11. Parallel diffusion coefficient, D_o,	(km^2/s)	0.12	0.12	0.12
12. Effective scale height, H_n,	(km)	30	22	30
13. Initial gravitational drift, $g\tau_o$,	(m/s)	8	10.9	8
14. Downward neutral wind, V_{D1},	(m/s)	0	8	0
Derived Quantities				
1. Neutral cloud radius, $\bar{a}$, at $t = t_i + \tau_i$	(km)	3.80	3.80	3.51
2. Neutral cloud radius at 20 s	(km)	4.72	4.72	4.42
3. Peak ion density at 22 s	$(10^{13}\ m^{-3})$	2.4	2.4	2.2
4. Maximum ion density	$(10^{13}\ m^{-3})$	2.45	2.45	2.30
5. Transverse scale size	(km)	2.66	2.66	2.30
6. Peak ion density at 100s	$(10^{13}\ m^{-3})$	1.75	1.75	1.6
7. Ion cloud length at 100s	(km)	7.8	7.8	7.6
8. Field line content	$(10^{17}\ m^{-2})$	2.4	2.4	2.16
9. Initial Pedersen conductivity	(mho)	27.4	27.4	24.7
10. Peak ion density at 30 min.	$(10^{13}\ m^{-3})$	0.57	0.70	0.51
11. Ion cloud length at 15 min.	(km)	18.5	16.0	18.5
12. Ion cloud length at 30 min.	(km)	24	19	24

with our present modeling and a reduced transverse scale size for the ion cloud. We believe that the modeling presented here is theoretically more well-founded and, as we shall see below, is more consistent with the existing observations.

However, this value of ion inventory is considerably larger than the value of 3.5×10^{24} derived by Tsunoda[21] based on measurements made with the incoherent-scatter radar. Since we will be making a detailed comparison of the results of models A, B and C with the model obtained from the incoherent-scatter radar, an evaluation of the reasons for the different values will be made at that time. The ion inventory for model C was arrived at specifically by an attempt to match the parameters determined by the incoherent-scatter radar. We believe that the model C value represents an actual underestimate of the total ion inventory as will be made clearer below.

A unique measurement of the ion inventory in the Plum ion cloud produced from a different 48 kilogram payload barium release at about 185 kilometers altitude during the Secede II test series was made by Prenatt.[22] Prenatt made dispersive-phase measurements by receiving, at four separate sites, several radio frequencies transmitted by a beacon passing behind the ion cloud. These measurements provided the total ion content along four cuts through the Plum ion cloud. These data were received during a time span from approximately 2 to 3 1/2 minutes after release. The Plum ion cloud was already quite distorted at this time, but Prenatt was able to successfully model the ionization content by superposing 3 different Gaussian distributions.

As a result of his modeling Prenatt determined a characteristic 1/e dimension transverse to the magnetic field of about 2.8 km and a total ion inventory of 7.4×10^{24}. Because Plum was released at a slightly lower altitude than Spruce and more oxidation of Ba by the larger ambient oxygen density could be expected, one might consider this value of ion inventory to be a lower limit for the Spruce ion cloud. It was the existence of this measurement that motivated us to adopt a value as large as 6.5×10^{24} for the ion inventory in model A of the Spruce ion cloud.

The value of the ionization time constant and fraction of atoms ionized, items 3 and 4 in Table 5.1, were discussed in Section 3. We have adopted the same values for all three models. Once the fraction of atoms ionized is assumed, the mass of the released barium vapor, M_o, is determined. The vaporization efficiency, item 2, is just the ratio of this mass to the total chemical payload weight. We see that the resulting values lie within the crude 5 to 10% efficiency estimates that are often discussed.

The atmospheric density model adopted determines items 6 and 7. The equal-mass-radius, a_o, is defined in Section 2 and derived from items 1 and 6. The initial expansion velocity, $\dot{R}_o$, affects the scale size of the neutral cloud and thus the ion cloud. Likewise the time chosen for the onset of photoionization, t_i, also effects the scale of the ion cloud and the shape of the density distribution transverse to the magnetic field. In Section 3 we indicated that a minimum value for t_i was 1.5 seconds. A maximum reasonable value must not be too much larger than 2 seconds because radar observations indicate that the peak electron concentration exceeds $7 \times 10^{12}\ m^{-3}$ within 3 seconds of release.[9] We shall defer discussion of the late-time inputs to the models until we discuss parameters derived from these inputs.

We now discuss the results obtained by applying the modeling concepts developed in the three previous sections and these input parameters to the Spruce ion cloud. We have already seen in Section 2 that the snowplow expansion model with diffusion added provides good agreement with a photograph of the neutral cloud at 20 seconds after release. We further indicated that diffusion rapidly causes the density profile to become Gaussian. Furthermore, the cloud radius determined by the snowplow is essentially equal to a point that has a density 1/e of the central density. Hence, we approximate the neutral cloud by an expanding Gaussian whose Gaussian radius is given by

$$a(t) = a_o \left[1.44 \left(\frac{\dot{R}_o t}{a_o} \right)^{0.8} - 0.63 \right] . \qquad (5.1)$$

In Section 3 we described the deposition of ionization on magnetic field lines. An appropriate scaling parameter was the radius, $\bar{a}$, of the neutral cloud at $t = t_i + \tau_i$, i.e., one photoionization time after photoionization is assumed to begin. The resulting values of $\bar{a}$ for the three models are listed as the first derived quantity in Table 5.1. The value of this radius is smaller for model C because the mass of the released vapor is smaller and the time at which photoionization commences, t_i , is earlier. The radius of the neutral cloud at 20 seconds after release is listed as the second derived quantity.

Figure 5.1 shows the results of the ion deposition calculation. The four solid curves show the total ion content on field lines as a function of the position across the magnetic field for several different times after release. For instance, the curve labeled $t = 5$ s represents the amount of ionization that has been deposited after photoionization has been operating for 3 s. The dashed curve, which we will discuss below, is a Gaussian profile. We observe, as remarked earlier, that the distribution of ionization on field lines by the deposition model is more peaked than a Gaussian. By 22 seconds after release, or 2 photoionization times τ_i , the total content is within 15% of the total content deposited on field lines.

The two dashed curves in Figure 5.1 show the field-line content at two separate times for model C. The total ion inventory indicated by the dashed curve labeled total content is approximately 2/3 of the total ion inventory contained within the solid curve labeled total content. The transverse scale size listed as the fifth derived quantity is the radius at which the total field line content has a value of 1/e of the field-line content passing through the center of the cloud.

Once an electron-ion pair is created, it is tied to the magnetic field line on which it originated. It can no longer expand across the magnetic field and the transverse scale size of the ion cloud is given by the distribution shown in Figure 5.1. There is no such restriction on the motion of the ions parallel to the magnetic field. During the first 20 seconds after release we

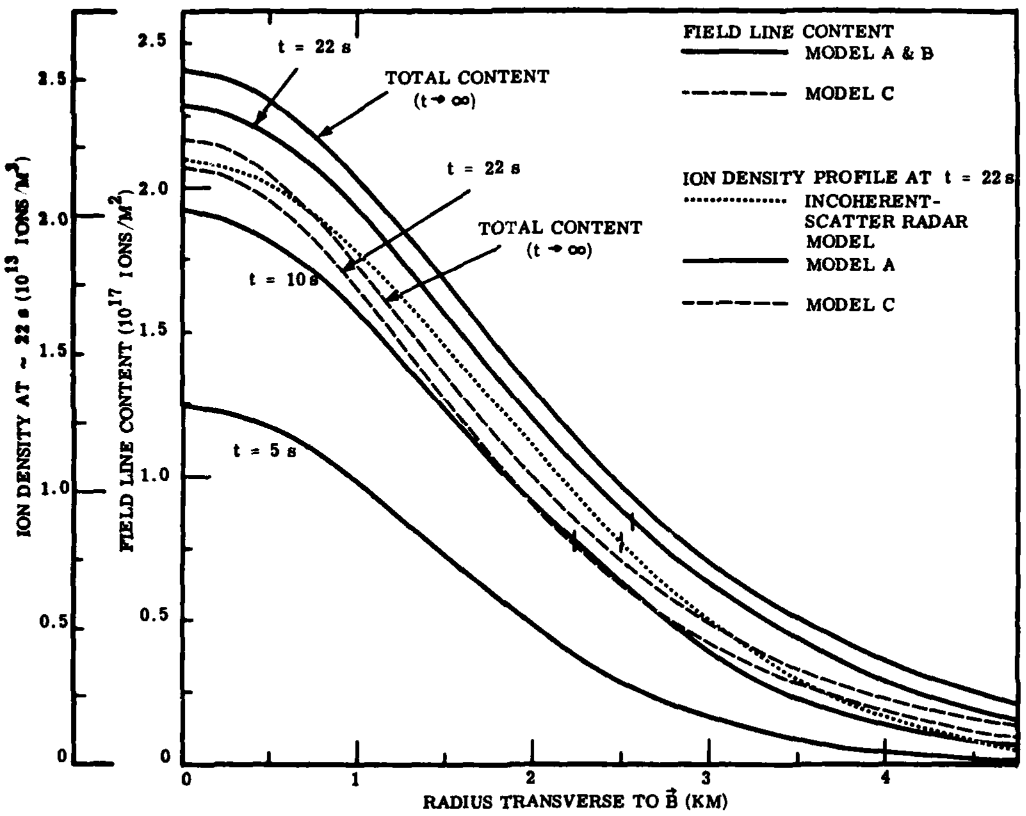

Figure 5.1. Ion deposition for Spruce according to models A, B, and C. The solid curves (dashed curves) show the field line content for four (two) different times after release for models A and B (model C) as a function of distance transverse to B. The solid and dashed curves at 22 seconds after release also give the ion density profiles transverse to $\vec{B}$ read on the far left scale. They can be compared with the density profile, shown dotted, derived from incoherent-scatter radar measurements. The short vertical lines mark the position on the density profiles where the density is 1/e of its peak value.

assume that the ion distribution parallel to the magnetic field is the same as that given by the neutral cloud from which the ionization originated. Knowing the content on the field line and the scale length parallel to the field given by Eq. (5.1) we can derive an ion concentration profile at approximately 22 seconds after release. The left-hand scale for the ion concentration should be read only for the solid and dashed curves labeled $t = 22$ s.

Also shown in Figure 5.1 by a dotted curve is the Gaussian model derived by Tsunoda[21] based on measurements with the incoherent-scatter radar. This dotted curve can be compared to the solid and dashed curves labeled $t = 22$ s. We see that the model C peak ion concentration agrees with the Tsunoda model value, but that its Gaussian dimension transverse to $\vec{B}$ is a bit small. Model A, on the other hand, has a peak ion concentration that exceeds the Tsunoda model value by approximately 10% but provides an excellent agreement with the measured scale size transverse to $\vec{B}$. If the ion cloud actually had the shape given by model C, the incoherent-scatter radar would probably have measured a lower peak ion concentration due to the finite beam width. It is for this reason that we believe model C represents an underestimate to the actual size of the ion cloud and that the actual ion inventory is in excess of the model C ion inventory of 4.5×10^{24} ions.

Ionization is 85% complete by 22 seconds and we assume that the ion cloud expands parallel to the magnetic field by diffusion, i.e., we assume that the expansion due to the snowplow ceases. The increase in length of the ion cloud along the magnetic field is shown by the dotted line in Figure 2.4. We note that this increase is not substantially different than that predicted by the snowplow without diffusion. Thus initially we can represent the increase in the Gaussian scale size of the ion cloud parallel to the magnetic field by

$$\ell(t) = \left[\ell^2(22) + 4\,D_0\,(t - 22)\right]^{\frac{1}{2}} \quad . \qquad (5.2)$$

The time-dependence of the total ion inventory is

$$N(t) = N_T \left[1 - \exp\left(-(t - t_i)/\tau_i\right)\right] \tag{5.3}$$

for $t > t_i$. We may develop a model for the time dependence of the peak ion concentration, n_p, initially by taking into account the increase due to the additional, remaining ionization, and the decrease due to diffusion parallel to the magnetic field. We obtain an expression of the form

$$n_p(t) = n_p(22) \frac{\ell(22)}{\ell(t)} \frac{N_T(t)}{N(22)} \tag{5.4}$$

from which the maximum peak ion density, listed as item 4 in Table 5.1, has been determined.

We have examined the evolution of the Spruce ion cloud as it settles under gravity. Figure 5.2 shows the development of the Spruce ion cloud according to model A. Initially, for the first 10 minutes, the peak ion concentration behaves according to Eq. (5.4). This equation is a valid description of the time dependence of the peak concentration because the ion cloud has not descended very far into the atmosphere and the diffusion coefficient, D_o, has essentially its initial value given by the input parameter item 11 in Table 5.1. The peak ion concentration and the ion cloud length at 100 seconds, listed as items 6 and 7 in Table 5.1, are given by Eqs. (5.4) and (5.2) respectively. At later time, however, when the parallel diffusion coefficient evaluated at the center of the ion cloud is different from its initial value, the peak ion concentration ceases to fall as rapidly as predicted by Eq. (5.4).

Figure 5.3 shows a plot of the peak ion concentration as a function of time after release. The late-time curve for model A results from the ion cloud settling under the influence of gravity. We note that the ion concentration has fallen below $7 \times 10^{12}\ m^{-3}$ by 18 minutes after release for model A. The short-pulse radar operated by Oetzel and Chang[23] continued receiving

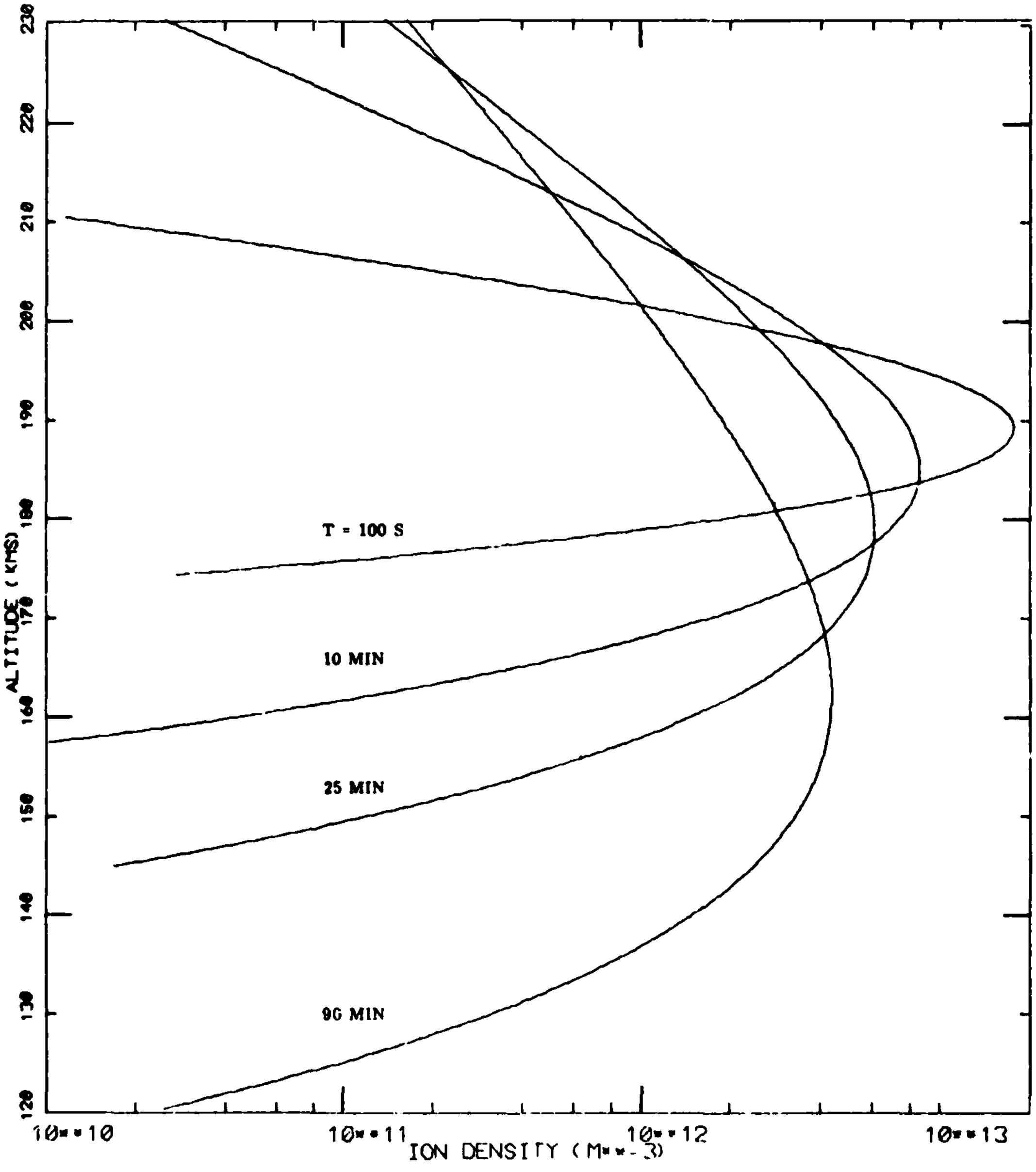

Figure 5. 2. Expansion and descent of the Spruce ion cloud for model A under the assumption of no winds and constant effective neutral density scale height. Times shown are times after release.

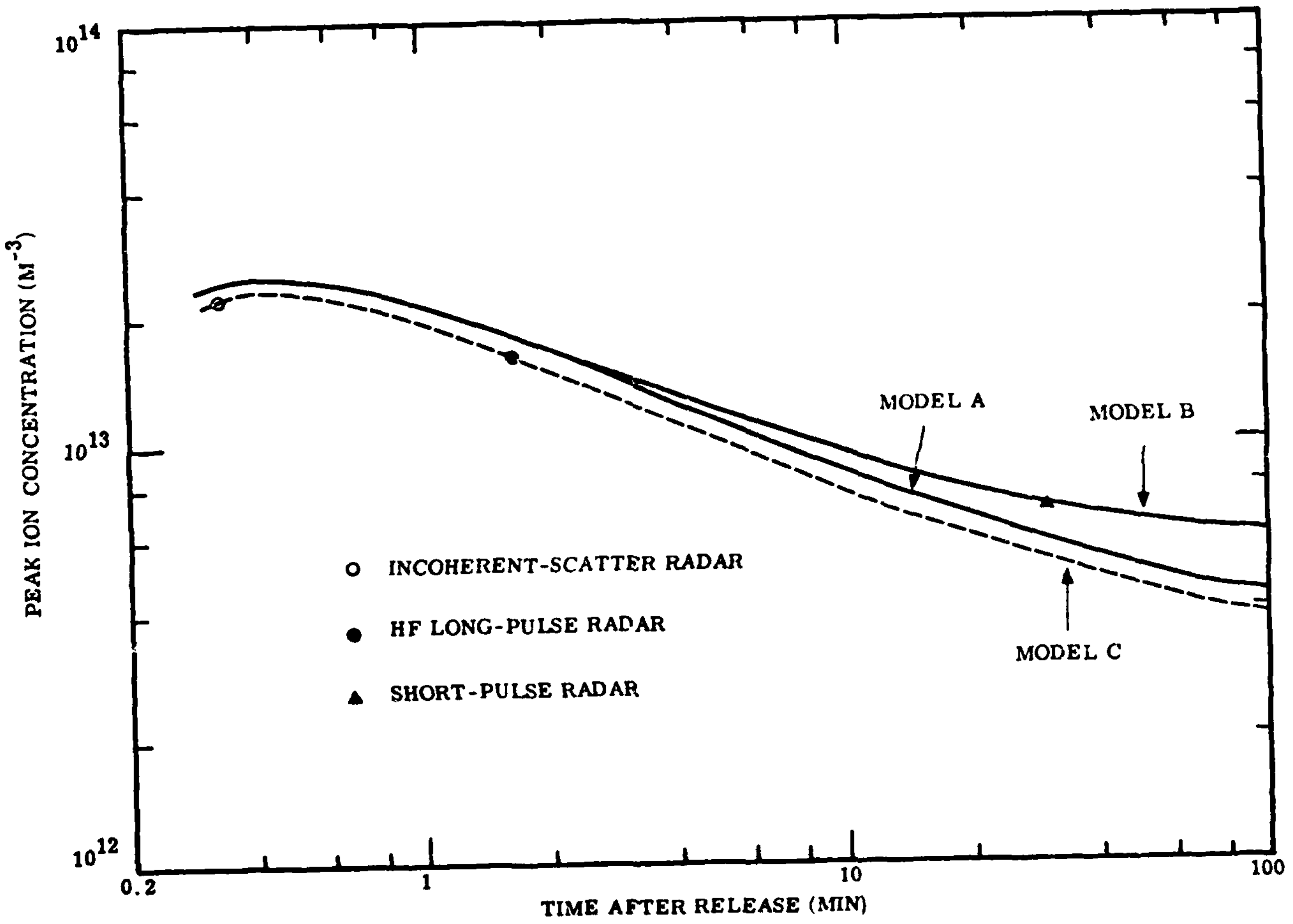

Figure 5.3. Peak ion concentration as a function of time after release as determined by models A, B, and C.

returns, although sporadically, at 24 MHz indicating the presence of an overdense cloud with an ion concentration of 7×10^{12} m^{-3} as late as 30 minutes after release.

Since downward winds, or a descent of the cloud to a region of cooler atmosphere where the atmospheric scale-height is less, decrease the effective diffusion coefficient, the ion cloud would not expand along the field line as rapidly as predicted by model A. In order to model this effect we adjusted the late-time input parameters for model B. We decreased the neutral density scale-height to 22 km (the same value used in Section 4 for the Anne ion cloud) and added a downward neutral wind of 8 m/s. In order to keep the initial diffusion coefficient the same in this cooler atmospheric model, we had to reduce the atmospheric density at 190 km by a small amount resulting in the increased value of $g \tau_0$. By making these changes we find that the model B curve does maintain the ion concentration above 7×10^{12} m^{-3} for more than 30 minutes.

We note that the model A and B peak ion concentration curves pass above the measurements made at 22 seconds and 100 seconds after release by two independent radar systems. The HF long-pulse-radar value[24] does provide only a lower bound to the peak concentration. Other 48 kg barium releases have indicated peak values at 100 seconds after release of between 1.6 and 1.9×10^{13} m^{-3}. It was primarily for this reason that the ion inventory for model A was chosen so that the model A curve would lie slightly above the measurement made at 100 s.

In model C the inventory was reduced so that the peak ion concentration would agree with these two early-time measurements. We have already indicated when we discussed Figure 5.1 why we feel that the density profile predicted by model C would actually give a measured value at 22 seconds less than the value that was measured. The model C curve essentially lies 10% below the model A curve.

Model B not only predicts a less rapid decrease in the peak ion concentration but it also predicts that the ion cloud Gaussian length parallel to the magnetic field does not increase so rapidly. The two solid curves in Figure 5.4 show the increase in Gaussian length as a function of time for models A and B respectively. By comparison, we have shown the increase in length predicted by Eq. (5.2) for two different values of the parallel diffusion coefficient as indicated by the two dashed curves. We note that for the first ten minutes after release there is little difference between the four curves. However, measurements of the full width of the ion cloud parallel to the magnetic field using the incoherent-scatter radar have indicated that by about 15 to 20 minutes after release the Gaussian length was 16 to 18 km and did not increase very rapidly after this time. This measurement, in addition to the short-pulse radar measurement, lends support to the model B description of the late-time behavior of the Spruce ion cloud.

The field-line-content for the three models is given as item 8 in Table 5.1. The initial field-line-integrated Pedersen conductivity, defined by Eq. (4.14), can be calculated from a knowledge of the field-line-content and is given as item 9 of Table 5.1. At later times, as the ion cloud descends, the Pedersen conductivity increases according to Eq. (4.57). The last three items in Table 5.1 list some of the late-time parameters derived from these three models.

The procedures that have been developed in Sections 2, 3 and 4 have provided a satisfactory explanation of many of the observations of the Spruce ion cloud. These procedures can be extended to model other ion clouds. The real test of the modeling concepts that have been developed here is to apply the model to ion clouds of different payloads released at different altitudes. So far this task has not been done. However, based on the success that we have achieved with this model, we are confident in applying it to other ion clouds of around 48 kg chemical payload weight released in the vicinity of 180 to 190 km altitude.

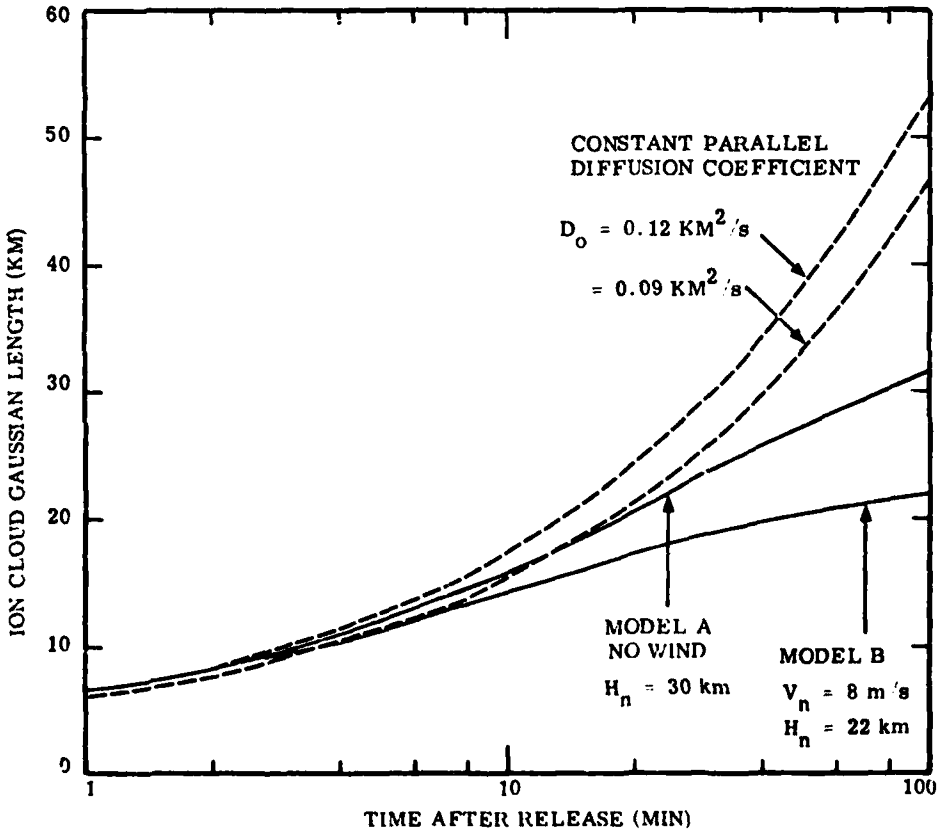

Figure 5.4. Spruce ion cloud Gaussian length parallel to the magnetic field as a function of time after release for models A and B as compared to the assumption of constant parallel diffusion coefficients.

6. LIST OF REFERENCES

1. Linson, L. M., "Quantitative Ion Cloud Modeling," in Analysis of Barium Clouds - Final Technical Report, RADC TR-72-335, Vol. I, pp. 1-39, Avco Everett Research Laboratory, Everett, Mass. 02149, October 1972.

2. Hoffman, H. S., and G. T. Best, "The Initial Behavior of High Altitude Barium Releases - II. The Expanding Vapor Cloud," J. Atmos. Terr. Phys., 36, 1475, 1974.

3. Stuart, G. W., "Explosions in Rarefied Atmospheres," Phys. Fluids, 8, 603, 1965.

4. Baxter, D. C., and L. M. Linson, "Dynamics of Gas Clouds Released at Satellite Orbital Velocity," in Rarefied Gas Dynamics, J. L. Potter, ed., Progress in Astronautics and Aeronautics, 51: Part 1, 477, 1977.

5. Alford, G. C., and R. N. Bybee, "Secede II Chemical Payloads," RADC-TR-71-232, pp. 1-21, Thiokol Chemical Corporation, Ogden, Utah, 84402, June 1971.

6. Boquist, W. P., R. W. Deuel, S. G. Hawks, P. L. Crawley, and D. E. Overbye, "High Resolution Optical Measurements of ARPA Project Secede II," RADC-TR-72-307, pp. 1-65, Technology International Corporation, Bedford, Mass., November 1972.

7. Haerendel, G., R. Lüst, and B. Meyer, "MPI Analysis of Observations," in Barium Releases at Altitudes Between 200 and 1000 Kilometers," NASA SP-264, pp. 15-46, 1971.

8. Rosenberg, N. W., G. T. Best, F. P. Delgreco, M. M. Klein, M. A. Macleod, T. M. Noel, W. K. Vickery, "AFCRL Barium Release Studies 1967," reissued as Special Report #4, pp. 1-48, Stanford Research Institute, Menlo Park, Calif. 94025, January 1969.

9. Oetzel, G. N., "An Electron-Density Model for Event Spruce and its Relationship to Short-Pulse-Radar Cross-Section Measurements," Special Report #17, pp. 1-25, Stanford Research Institute, Menlo Park, Calif. 94025, September 1972.

10. Chavin, S., and R. W. Kilb, personal communication, January 1977.

11. Perkins, F. W., N. J. Zabusky, and J. H. Doles III, "Deformation and Striation of Plasma Clouds in the Ionosphere, 1," J. Geophys. Res. 78, 697, 1973.

12. Perkins, F., "Spread F and Ionospheric Currents," J. Geophys. Res., 78, 218, 1973.

13. Scannapieco, A. J., S. L. Ossakow, D. L. Book, B. E. McDonald, and S. R. Goldman, "Conductivity Ratio Effects on the Drift and Deformation of F Region Barium Clouds Couplied to the E Region Ionosphere," J. J. Geophys. Res., 79, 2913, 1974.

14. Haerendel, G., R. Lüst, and E. Rieger, "Motion of Artificial Ion Clouds in the Upper Atmosphere," Planet. Space Sci., 15, 1, 1967.

15. Linson, L. M., "Motion of Barium Ion Clouds," in Analysis of Barium Ion Clouds, RADC TR-72-103, Vol. I, p. 39, Avco Everett Research Laboratory, Everett, Mass. 02149, January 1972.

16. Linson, L. M., "Effect of Conjugate Ionosphere and Shape on the Motion of Barium Ion Clouds," Trans., Am. Geophys. Union, 52, 880, 1971.

17. Yu, K., and M. M. Klein, "Diffusion of Small Particles in a Nonuniform Atmosphere," Phys. Fluid, 7, 651, 1964.

18. Handbook of Mathematical Functions with Formulas, Graphs, and Mathematical Tables, M. Abramowitz and I. A. Stegun, eds. National Bureau of Standards Applied Mathematics Series-55, Washington, D.C., 1965.

19. Rao, P. B., "A Diffusion Model for the Electron Density Distribution Along the Earth's Magnetic Field in an F-Region Plasma Cloud," J. Atmos. and Terr. Phys., 35, 795, 1973.

20. Mitchell, J. H., and K. E. W. Ridler, "The Speed of Positive Ions in Nitrogen," Proc. Roy. Soc., (London), A146, 911, 1934.

21. Tsunoda, R. T., "Incoherent-Scatter Results for Event Spruce," in Proc. of the SECEDE II Final Data Review Meeting, RADC TR-72-153, Vol. II, p. 111, Stanford Research Institute, Menlo Park, Calif. 94025, May 1972.

22. Prenatt, R. E., "A Preliminary Model for the Electron Concentration in the Early Plum Ion Cloud," in Proc. of the SECEDE II Final Data Review Meeting, RADC TR-72-153, Vol. II, p. 285, Stanford Research Institute, Menlo Park, Calif. 94025, May 1972.

23. Oetzel, G. N., and N. J. F. Chang, "Results of the Secede II Short-Pulse Radar Experiment," RADC TR-72-218, Stanford Research Institute, Menlo Park, Calif. 94025, June 1972.

24. Thome, G., personal communication, 1971.

DISTRIBUTION LIST

DEPARTMENT OF DEFENSE

Director
Command Control Technical Center
ATTN: C-650

Director
Defense Advanced Rsch. Proj. Agency
ATTN: Nuclear Monitoring Research
ATTN: Strategic Tech. Office

Defense Communication Engineer Center
ATTN: Code R410, James W. McLean
ATTN: Code R820, R. L. Crawford

Director
Defense Communications Agency
ATTN: Maurey Raffensperger
ATTN: Code 101B, Major Rood
ATTN: Code 480
ATTN: Code 810, R. W. Rostron

Defense Communications Agency
WWMCCS System Engineering Org.
ATTN: R. L. Crawford

Defense Documentation Center
12 cy ATTN: TC

Director
Defense Nuclear Agency
ATTN: TISI, Archives
ATTN: DDST
ATTN: STVL
3 cy ATTN: RAAE
3 cy ATTN: TITL, Tech. Library

Commander
Field Command
Defense Nuclear Agency
ATTN: FCPR

Director
Interservice Nuclear Weapons School
ATTN: Doc. Control

Director
Joint Strat. Tgt. Planning Staff
ATTN: JLTW-2

Chief
Livermore Division, Fld. Command, DNA
Lawrence Livermore Laboratory
ATTN: FCPRL

Director, National Security Agency
ATTN: W14, Pat Clark
ATTN: John Skillman, R52

OJCS/J-3
ATTN: WWMCCS, Eval. Ofc. Mr. Toma

Under Sec'y of Def. for Rsch. & Engrg.
ATTN: S&SS (OS)

DEPARTMENT OF THE ARMY

Director
BMD Advanced Tech. Ctr.
ATTN: ATC-T, Melvin T. Capps

Commander
Harry Diamond Laboratories
ATTN: DRXDO-TI, Mildred H. Weiner
ATTN: DELHD-NP, Francis N. Wimenitz
ATTN: DELHD-NP

Director
TRASANA
ATTN: ATAA-SA

Commander
U.S. Army Comm-Elec. Engrg. Instal. Agy.
ATTN: EED-PED, George Lane

Commander
U.S. Army Foreign Science & Tech. Ctr.
ATTN: P. A. Crowley

Commander
U.S. Army Nuclear Agency
ATTN: MONA-WE, J. Berberet

Commander
U.S. Army SATCOM Agency
ATTN: Doc. Control

DEPARTMENT OF THE NAVY

Chief of Naval Operations
ATTN: OP 943, LCDR Huff
ATTN: Ronald E. Pitkin
ATTN: Alexander Brandt

Chief of Naval Research
ATTN: Code 461

Commanding Officer
Naval Intelligence Support Ctr.
ATTN: Mr. Dubbin, STIC 12

Commander
Naval Ocean Systems Center
ATTN: Code 2200

Director
Naval Research Laboratory
ATTN: Code 5400, HG. Comm. Dir., Bruce Wald
ATTN: Code 7700, Timothy P. Coffey
ATTN: Code 7701, Jack D. Brown
ATTN: Code 5430, Satellite Comm.

Officer-in-Charge
Naval Surface Weapons Center
ATTN: Code WA501, Navy Nuc. Prgms. Off.

Director, Strategic Sys. Proj. Office
ATTN: NSSP-2722, Fred Wimberly
ATTN: NSP-2141

[redacted]

DEPARTMENT OF THE AIR FORCE

AF Geophysics Laboratory, AFSC
ATTN: PHD, John P. Mullen
ATTN: OPR, James C. Ulwick
ATTN: PHD, Jurgen Buchau
ATTN: SUOL, Rsch. Library
ATTN: PHP, Jules Aarons

AF Weapons Laboratory, AFSC
ATTN: SUL
ATTN: SAS, John M. Kamm
ATTN: DYC, Capt L. Wittwer

AFTAC
ATTN: TN

Air Force Avionics Laboratory, AFSC
ATTN: AAD, Allen Johnson

Headquarters
Electronic Systems Division (AFSC)
ATTN: Jim Deas

Commander
Foreign Technology Division, AFSC
ATTN: NICD, Library

Commander
Rome Air Development Center, AFSC
ATTN: EMTLD, Doc. Library

SAMSO/MN
ATTN: MNNL, Lt Col Kennedy

SAMSO/SK
ATTN: SKA, Lt Maria A. Clavin

SAMSO/YA
ATTN: YAT, Capt L. Blackwelder

Commander In Chief
Strategic Air Command
ATTN: NRT
ATTN: ADWATE, Capt Bruce Bauer
ATTN: XPFS, Maj Brian G. Stephan

DEPARTMENT OF ENERGY

University of California
Lawrence Livermore Laboratory
ATTN: Tech. Info. Dept., L-3

Los Alamos Scientific Laboratory
ATTN: Doc. Con. for John Zinn
ATTN: Doc. Con. for Robert Jeffries

Sandia Laboratories
ATTN: Doc. Con. for D. A. Dahlgren, Org. 1722
ATTN: Doc. Con. for W. D. Brown, Org. 1353
ATTN: Doc. Con. for J. P. Martin, Org. 1732
ATTN: Doc. Con. for T. Wright

OTHER GOVERNMENT AGENCIES

Department of Commerce
Office of Telecommunications
ATTN: William F Utlaut

NASA, Goddard Space Flight Center
ATTN ATS-6, Ofc R Corrigan

OTHER GOVERNMENT AGENCIES (Continued)

National Oceanic & Atmospheric Admin.
Environmental Research Laboratories
ATTN: C. L. Rufenach

DEPARTMENT OF DEFENSE CONTRACTORS

Aerospace Corporation
ATTN: Norman D. Stockwell
ATTN: SMFA for PWW
ATTN: Irving M. Garfunkel
ATTN: J. E. Carter, 120, Rm. 2209

The Boeing Company
ATTN: D. Murray
ATTN: Glen Keister

University of California at San Diego
Marine Physical Lab. of the Scripps
ATTN: Henry G. Booker

Charles Stark Draper Laboratory, Inc.
ATTN: J. P. Gilmore, MS 63
ATTN: D. B. Cox

Computer Sciences Corporation
ATTN: H. Blank

Comsat Laboratories
ATTN: R. R. Taur

Cornell University
Dept. of Electrical Engineering
ATTN: D. T. Farley, Jr.

ESL. Inc.
ATTN: James Marshall
ATTN: C. W. Prettie

General Electric Company
TEMPO-Center for Advanced Studies
ATTN: Warren S. Knapp
ATTN: DASIAC

General Electric Company
ATTN: F. A. Reibert

General Research Corporation
ATTN: John Ise, Jr.
ATTN: Joel Garbarino

Geophysical Institute
University of Alaska
ATTN: Tech. Library

University of Illinois
Dept. of Electrical Engineering
ATTN: K. C. Yeh

Institute for Defense Analyses
ATTN: Ernest Bauer

Intl. Tel. & Telegraph Corporation
ATTN: Tech. Library

JAYCOR
ATTN: S. R. Goldman

Linkabit Corporation
ATTN Irwin Jacobs